Fall 11-14-2019

INTEGRATED CHIRPED-GRATING SPECTROMETER-ON-A-CHIP

Shima Nezhadbadeh
University of New Mexico

Shima Nezhadbadeh

Candidate

Physics and Astronomy

Department

This dissertation is approved, and it is acceptable in quality and form for publication:

Approved by the Dissertation Committee:

Dr. Steven R.J. Brueck, Chairperson

Dr. Payman Zarkesh-Ha

Dr. Tito Busani

Dr. Arash Mafi

INTEGRATED CHIRPED-GRATING SPECTROMETER-ON-A-CHIP

by

SHIMA NEZHADBADEH

M.S. in Optical Science and Engineering, The University of New Mexico, 2015

DISSERTATION

Submitted in Partial Fulfillment of the
Requirements for the Degree of

Doctor of Philosophy
Physics

The University of New Mexico
Albuquerque, New Mexico

December 2019

To
my spouse, Ryan Chapman
for unconditional support, encouragement and patience through all these years.

Acknowledgments

I would like to thank my advisor, distinguished Professor Steven R. J. Brueck, for his supports, streaming knowledge, expertise and insightful guidance through all these years of my study and work in his research group. I can't imagine a better mentor for my graduate study and research.

I am also deeply grateful to my committee member, professor Payman Zarkesh-Ha for his advices, guidance and supports.

I also want to thank Dr. Alexander Neumann for his contribution to the device characterization work as well as helps in chirped grating fabrication in this project.

Finally, I would like to thank other group members and all other faculty, staff and students at CHTM for their help and friendship.

INTEGRATED CHIRPED-GRATING SPECTROMETER-ON-A-CHIP

SHIMA NEZHADBADEH

M.S. in Optical Science and Engineering, The University of New Mexico, 2015

Ph.D. in Optical Science and Engineering, The University of New Mexico, 2019

Abstract

In this dissertation we demonstrate a new structure based on waveguide coupling atop a silicon wafer using a chirped grating to provide the dispersion that leads to a high-resolution, compact, fully integrable and CMOS-compatible spectrometer. Light is both analyzed and detected in a single, completely monolithic component which enables realizing a high-resolution portable spectrometer with an extremely compact footprint. The structure is comprised of a $SiO_2/Si_3N_4/SiO_2$ waveguide on top of a silicon wafer. Grating regions are fabricated on the top cladding of the waveguide. The input light is incident on a chirped grating area known as the collection area. Because of the local variation of the grating pitch across the collection area, different wavelengths of light are coupled into the waveguide at different lateral positions across the collection area. Guided light is then outcoupled through second grating region known as the detection area to the array of photodiodes placed either atop the second grating region or below the second grating region in silicon chip. Therefore, spectral information is encoded in the chirped grating coupler, which is fabricated in a single lithography step, independent of the number of channels. For these initial experiments, a separate detection array was used. In future iterations, these detectors can be integrated into the underlying silicon, resulting in a fully integrated spectrometer on a chip. Varying the input angle of the light will vary the measurement

spectral range. This will result in an inexpensive spectrometer on chip, with adjustable resolution and spectral coverage controlled by the grating chirp and the input angle.

Contents

Chapter1

1.1 Introduction

A spectrum is a measure of the intensity of light as a function of wavelength or energy. A rainbow is basically a spectrum that is caused by dispersion of solar radiation in water droplets resulting in a spectrum of the light appearing in the sky. The spectrum of light source contains information on how the optical energy or power is distributed over different wavelengths.

Optical spectra can be recorded with instruments which are called optical spectrometers. These spectrometers utilize the phenomenon of optical dispersion. The measured spectra of materials using spectrometers give us data on the structure and properties of matter, which is used for solving a wide variety of analytical problems from estimating the composition of distant objects in our universe to how much blue light (which can hinder sleep at night) is emitted from a white-light LED.

A spectrometer is a scientific instrument used to separate and measure spectral components of the light. The basic design of a spectrometer using for chemical and biological sensing has four basic components: detector, light discrimination component, light source, and sample interface[1], [2].

There are a wide variety of detectors that are used for the optical sensing. Today we find single element detectors and multielement detector arrays that respond from the ultraviolet portion of the spectrum into the far infrared. The detection of optical radiation is accomplished by converting photon energy into an electrical signal through the use of photosensitive materials and thermally responsive materials. Since detectors and light sources alone cannot discriminate wavelength, it is necessary to add another component to the optical system: wavelength separation. Wavelength discrimination can be accomplished in a variety of ways. Diffraction of light can be realized using optical or mechanical means. Discrete or variable optical filters isolate wavelength by transmitting very specific portions of the electromagnetic spectrum. Diffraction of light can be accomplished using a grating, which is a series of spatially micromachined grooves on a substrate or by projecting light through a prism.

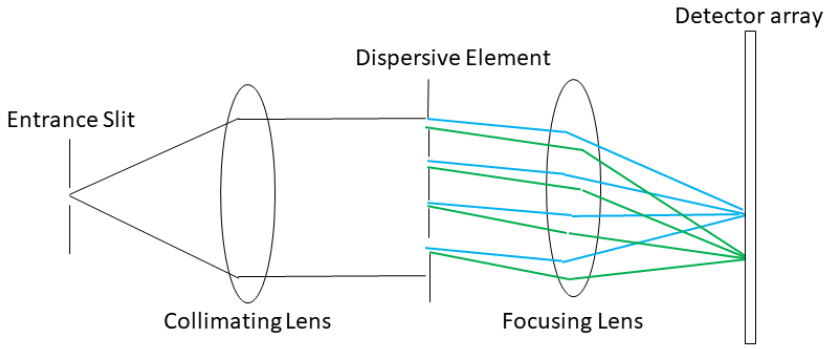

Figure 1-1:Simplified schematic of the basic spectrometer in case of a grating and with two spectral components separated.

1.2 Spectrometer Parameters

Some of the key parameters for comparing different spectrometers are[3]:

- The spectral range is the range of wavelengths in which the spectrometer operates.
- The resolution which is the minimum feature size that can be distinguished in the spectrum, often described as the minimum spacing between two peaks such that they can be resolved as separate.
- The signal-to-noise ratio and stray light level requirements
- The dynamic range requirements
- The linearity requirements
- Etendue (throughput) is a measure of how much light can be coupled into a spectrometer and is given by the area of the input slit times the numerical aperture.
- The physical size of the spectrometer

A spectrometer can in general not be optimized for all parameters, so it is important to compare only spectrometers that are designed for the same application.

1.3 Conventional Spectrometer

The classification of the various spectrometer types is determined by the dispersion element or approach used and includes spectrometers based on (a) prisms, (b)gratings and (c) interference of split components[2].

1.3.1 Spectrometers Based on Dispersion

The instrument that reads the electro-magnetic spectrum by separating the incoming light into a number of spectral channels and detecting them individually is called a spectrometer. In common lab spectrometers that operate in the visible and infrared parts of the electromagnetic spectrum, this process is done by spatially separating the input light into components of a certain spectral width using a dispersion element such as a grating or a prism, which are subsequently detected on a single detector (with a rotating grating) or on a 1D-array of fixed photodetectors.

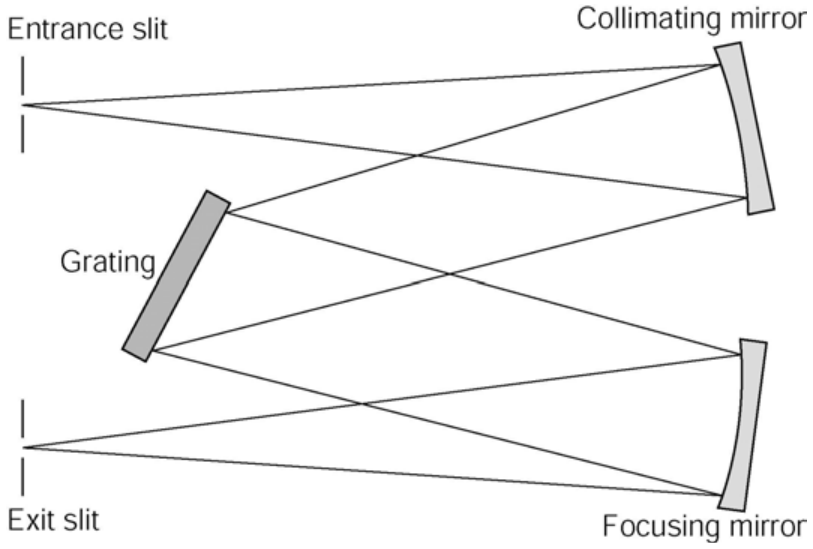

Figure 1-2: Simplified schematic of the grating-based spectrometer.

Spectrometers based on dispersion are basically composed of the following components[4]:

- An input slit for spatial sampling of the radiation; This slit is critical to the spectrometer's performance and determines the amount of light that enters the optical bench and is a driving force when determining the spectral resolution. The optical resolution and throughput of a spectrometer will ultimately be determined by width of the slit.

- A collimating lens (mirror) to produce a collimated light beam; Collimating lenses are optical lenses that help to make parallel the light that enters the spectrometer setup. These lenses allow users to control the field of view, collection efficiency and spatial resolution of their setup, and to configure illumination and collection angles for sampling.
- A dispersion element, in case of a grating, it diffracts the different wavelengths presented in the light beam to different angles; The diffraction grating of a spectrometer determines the wavelength range and partially determines the optical resolution that the spectrometer will achieve.
- Groove Frequency: The amount of dispersion is determined by the number of grooves per mm ruled into the grating. This is commonly referred to as groove density, or groove frequency. The groove frequency of the grating determines the spectrometer's wavelength coverage and is also a major factor in the spectral resolution. The wavelength coverage of a spectrometer is inversely proportional to the dispersion of the grating due to its fixed geometry. However, the greater the dispersion, the greater the resolving power of the spectrometer. Inversely, decreasing the groove frequency decreases the dispersion and increases wavelength coverage at the cost of spectral resolution. When the required wavelength coverage is over an octave, i.e. $\lambda_{max} > 2\lambda_{min}$, optical signals in wavelengths from different diffraction orders may end up at the same spatial position on the detector plane, which will become evident once we take a look at the grating equation. In this case, a linear variable filter (LVF) is required to eliminate any unwanted contributions or perform "order sorting".

- A focusing lens that produces an image of the input slit in the plane of the sensor with the position of the image depending on the wavelength.
- And a detector or array of detectors.

As you can see dispersion-based spectrometer inherently is a multi-component system that is complex, expensive to manufacture, and potentially suffers from alignment degradation or malfunction, or problems with stray light that ultimately limit spectrometer performance.

1.3.2 Spectrometers Based on Interference

Interference-based spectrometers involve splitting of the incident light beam into two parts and having these interfere after travelling over two optical paths with a well-defined difference in length. The path length difference relative to the wavelength is an effective approach for selecting a spectral component. Changing the path length difference in time can be used for a complete spectral scan of a well-defined part of the spectrum. There are a number of variations on this general operating principle and Fig.1-3 shows the three most-widely used interferometers[2].

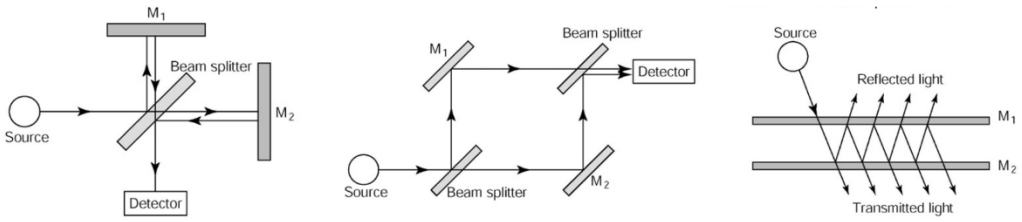

Figure 1-3:Operating principle of most-frequently used interferometer-based spectrometers: (a) Michelson, (b) Mach–Zehnder and (c) Fabry–Perot.

The Michelson interferometer uses one beam splitter and two mirrors (M_1 and M_2) to define the two optical paths. The difference in distance between the splitter and the mirrors defines the optical path length difference. Measuring the path length increase between the positions for two maxima or minima of the interference pattern detected at the detector by displacing

one of the mirrors in the direction of the optical axis provides the measured wavelength of the incident light. The Mach–Zehnder uses two splitters and provides a better isolation between input and output.

A Fabry-Perot spectrometer[5],[6] relies on an optical cavity to transmit a narrow wavelength band to a detector. If the cavity length is varied spatially and placed over a linear array of detectors, it behaves as a variable filter. With proper control of the cavity length, impressive resolution is attainable. Unfortunately, the cavity will reflect much of the input light, so throughput is poor. The cavity also limits the spectral range, so this design is typically used in applications with a known, relatively narrow spectral range of interest. It is well-suited to and commonly used in telecommunications applications, but not preferable for broadband sensing.

1.3.3 Fourier Transform Spectrometer

Fourier transform spectroscopy (FTS) is an interference-based interferometer. The basis of this technique is the Fourier-pair relationship between the interferogram of a sample and its spectrum. A Fourier-transform (FT) spectrometer generates the spectrum of its source radiation by modulating the radiation in the time domain through interference, which is then Fourier transformed. In a Fourier transform instrument, the diffraction grating is replaced by a Michelson interferometer, which works by splitting the beam from the sample into two and introducing a varying path difference, p, into one of them. When the two components recombine, there is a phase difference between them, and they interfere either constructively or destructively depending on the difference in path lengths[7]. The detected signal oscillates as the two components alternately come into and out of phase as the path difference is changed. If the radiation has wavenumber $\overline{\nu}$, the intensity of the

detected signal due to radiation in the range of wavenumbers $\bar{\nu}$ to $\bar{\nu} + d\bar{\nu}$, which we denote $I(p, \bar{\nu})d\bar{\nu}$, varies with p as

$$I(p, \bar{\nu})d\bar{\nu} = I(\nu)(1 + \cos 2\pi\bar{\nu}p)d\bar{\nu} \qquad (1\text{-}1)$$

Hence, the interferometer converts the presence of a particular wavenumber component in the signal into a variation in intensity of the radiation reaching the detector. An actual signal consists of radiation spanning a large number of wavenumbers, and the total intensity at the detector, which we write $I(p)$, is the sum of contributions from all the wavenumbers present in the signal:

$$I(p) = \int_0^\infty I(p, \bar{\nu})d\bar{\nu} = \int_0^\infty I(\bar{\nu})(1 + \cos 2\pi\bar{\nu}p)d\bar{\nu} \qquad (1\text{-}2)$$

The problem is to find $I(\bar{\nu})$, the variation of intensity with wavenumber, which is the spectrum we require, from the record of values of $I(p)$. This step is a standard technique of mathematics and is the 'Fourier transformation' step from which this form of spectroscopy takes its name. Specifically:

$$I(\bar{\nu}) = 4\int_0^\infty \{I(p) - \frac{1}{2}I(0)\}\cos 2\pi\bar{\nu}p \ dp \qquad (1\text{-}3)$$

where $I(0)$ is given by equation (1-2) with $p = 0$. This integration is carried out numerically in a computer connected to the spectrometer, and the output, $I(\bar{\nu})$ is the transmission spectrum of the sample.

The resolution of Fourier transform spectrometers is determined by the maximum path length difference, p_{max}, of the interferometer:

$$\Delta\bar{\nu} = \frac{1}{2p_{max}} \qquad (1\text{-}4)$$

For example, to achieve a resolution of 0.1 cm^{-1}, it requires a maximum path length difference of 5 cm.

The primary advantages of FTS compared to dispersive spectrometers are high optical throughput thereby greater signal-to-noise ratio, compact size, and relatively easily attainable high resolution which is constant over the entire spectral region as determined by the mirror displacement from the origin. Beside the large throughput, an additional benefit of the Fourier-transform spectrometers compared to grating-based devices is that the spectral information is measured at all wavelengths simultaneously[8].

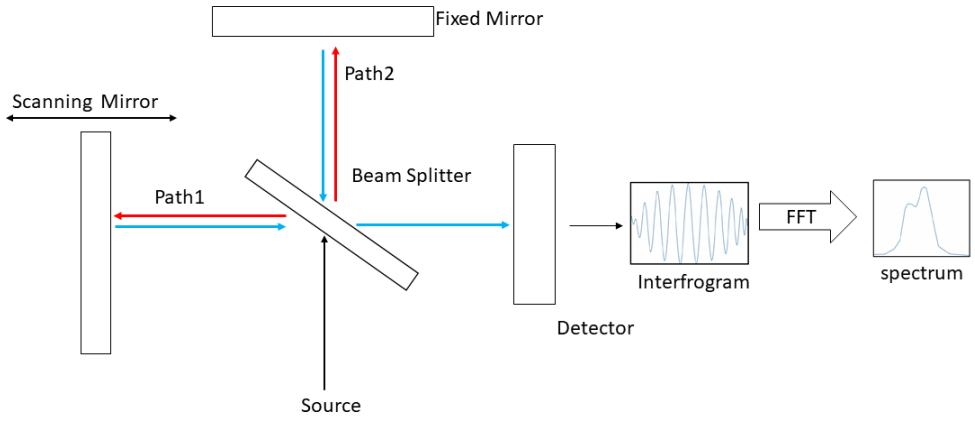

Figure 1-4: Fourier transform spectrometer is a Michelson interferometer with a movable mirror. By scanning the movable mirror over some distance, an interference pattern is produced that that encodes the spectrum of the source.

Although FTS can be more compact in size, its scanning interferometric configuration makes it slow for some applications where speed is a critical constraint. Spatial heterodyne spectroscopy (SHS) is an interferometric Fourier-transform (FT) technique based on a modified Michelson interferometer with no moving parts and relying on analysis of stationary interference patterns[9], [10].

1.3.4 Spatial Heterodyne Spectrometer

SHS is a method of Fourier transform spectroscopy based on a Michelson interferometer modified by replacing the mirrors in each arm with fixed diffraction gratings as shown in Fig.1-5.

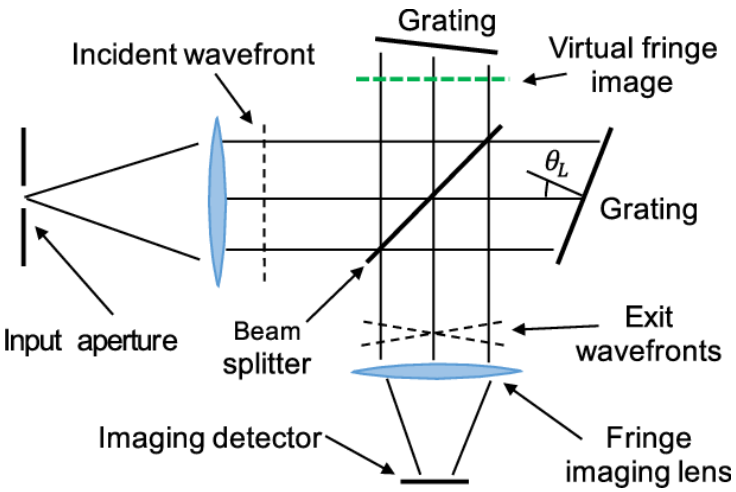

Figure 1-5: Conceptual drawing of the spatial heterodyne spectroscopy technique.

It uses a Michelson type interferometer, but it samples the entire interferogram simultaneously in the spatial domain without the need for moving parts. The gratings create a wavelength-dependent crossing angle between the recombined wavefronts that exit the interferometer. The interference of these wavefronts results in a Fizeau fringe pattern (interferogram) that is composed of wavelength dependent spatial frequencies that are heterodyned around the Littrow wavelength of the gratings. This is described by the output interferogram equation for the SHS,

$$I(x) = \int d\sigma B(\sigma)[1 + \cos(2\pi(4(\sigma - \sigma_L)x\tan\theta_L))] \qquad (1\text{-}5)$$

were $B(\sigma)$ is the input spectrum, $I(x)$ is the intensity across the detector plane, and σ_L and $\theta_L$are the Littrow angle and wavenumber, respectively. The virtual image of the fringes is localized near the grating faces and is imaged to a detector by the exit optics[11].

One of the advantages over the stepped Michelson are that SHS has no need for moving parts.

1.4 Spectrometer on Chip Approaches

Miniaturization of light sources and optical components increased the potential for the transformation of the benchtop spectrometers into a portable, handheld form which allows the spectrometer to leave the lab and enter the field for real-time material analysis.

Chip based Spectrometer uses a single component to undertake both the primary functions of a spectrometer: dispersion and detection.

When miniaturizing a spectrometer, one problem intrinsic to the device design arises: Resolution typically correlates with the size of the device: The bigger the device, the better the resolution. The difficulty of reducing spectrometer size arises from the fact that a long propagation path is needed for light of similar wavelengths to accumulate a detectable difference in phase. A solution to the resolution-size trade-off lies in folding the optical path inside a cavity, such as photonic-crystal cavities[12] , microdonut[13] , and micro-ring resonators[14]–[16].

Chip-based spectrometers, can be broadly classified into fiber/waveguide input and free-space input categories. Wavelength division multiplex telecommunications at NIR wavelengths is the focus of most of the fiber/waveguide applications whereas spectroscopy is the major application for spectrometers with free-space inputs. The spectrometers with fiber/waveguide input have limited applications, because they require delicate couplers and do not offer spatial information. On the other hand, free-space coupled devices offer much broader use such as imaging[17].

1.5 Examples of Spectrometers with Fiber/Waveguide Input

For fiber/waveguide input spectrometers, planar waveguide spectrometers based on echelle gratings[18], [19] and arrayed waveguide gratings[20], [21] have been designed and fabricated with sub-nanometer spectral resolution and very compact chip sizes. In array waveguide grating spectrometer, the core element of the device is an arrayed-waveguide grating (AWG). AWG is a wavelength separating and wavelength combining device. It couples light via a free-propagation region in a slab waveguide to an array of channel waveguides with a defined optical-path-length difference between adjacent channels, such that the wavelength dependent phase distribution at the array output causes different wavelengths to be diffracted to different locations, at which the pixels of a detector array can be positioned.

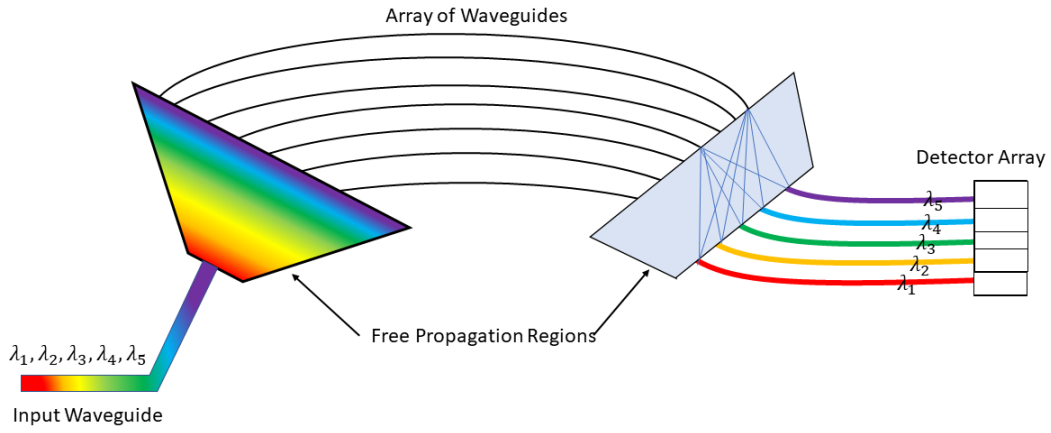

Figure 1-6: Schematics of an AWG spectrometer: The incoming light traverses a free space and enters a bundle of channel waveguides. The waveguides have different length and thus apply a different phase shift at the exit of the waveguides.The light then traverses another free space and interferes at the entries of the output waveguides in such a way that each output channel receives only light of a certain wavelength[22].

The spectral resolution of an AWG can be raised by increasing the interference order of the grating or the number of arrayed waveguides. However, increasing the grating order alone also reduces the free spectral range and therefore limits the usable bandwidth of the

spectrometer.

If we compare AWG and Echelle diffraction grating (EDG) spectrometers, an EDG is a grating mirror with step-shaped grooves with narrow facets in which the incident light is diffracted back, so only one FPR is required. This makes the EDG more compact.

Planar waveguide devices can achieve a high spectral resolution for a small device footprint, but their optical throughput is largely limited by the requirement of a single mode input waveguide. Throughput is of critical importance for spectroscopy applications, especially when spatially extended and incoherent sources are analyzed.

In Table 1-1 different AWG and EDG demonstrations are compared based on their footprint, central wavelength, sensing range, resolution.

Table 1-1:Examples of waveguide coupled spectrometers on chip.

Ref	Technology	Footprint	λ_c(nm)	$\Delta\lambda$(nm)	$\delta\lambda$(nm)
[22]	AWG with PD array/SOI	1×2 mm^2	2200	40	3
[23]	DeMUX grating/ Si-SiO_2	10×34 mm^2	1550	34.8	0.18
[19]	Echelle grating/ SOI	250×200 μm^2	1550	25.6	1.8

The implementations[22],[23],[19] were envisioned for application in wavelength division multiplexing (WDM) as demultiplexing elements. They offer resolution~ 1 nm, over a $25-40$ nm spectral range within a large $\sim mm^2$ footprint (except for ref.[19]where a very compact 0.2×0.2 mm^2 Echelle grating is used).

The spectral resolution of grating-based spectrometers scales with the optical path length, which translates to the linear dimension or footprint of the system. As a result, on-chip spectrometers based on curved gratings (Echelle) and arrayed waveguide gratings require relatively large footprints $(1-2\ \mathrm{cm})$. This limitation inspired researchers to develop a number of alternative spectrometer designs such as Dispersive photonic crystal lattice[24], microrings and microdoughnuts[13].

Another interesting approach in waveguide coupled spectrometers is based on a dispersive photonic-crystal lattice that generates extremely large angular dispersion in a small area[24]. In this approach, a combination of negative refraction and diffraction compensation in a super prism-based photonic crystal structure is used to demonstrate a compact on-chip photonic crystal spectrometer. This structure provides strong dispersion and signal isolation, which are essential for forming an efficient and compact spectrometer. The experimental results have shown that a PC structure with $80\ \mu\mathrm{m} \times 220\ \mu\mathrm{m}$ dimension can locate a single spectral feature with better than 10 pm accuracy over a bandwidth of 50 nm around 1550 nm center wavelength at an output signal-to-noise ratio of 13 dB[24].

The operation principle of the spectrometer based on dispersive photonic-crystal lattice is schematically shown in Fig.1-7(a)[25]. Input signals at different wavelengths are separated in angle upon entering the PC because of the super prism effect. The super prism effect is an effect observed in photonic crystal structures whereby the direction of light propagation is extremely sensitive to the wavelength and angle of incidence. The signals at different wavelengths then get focused while propagating inside the PC through the negative diffraction effect. The desired signals are also refracted in the negative refraction regime

and are separated from the stray light. The output of the PC device is sampled by an array of waveguides as shown in Fig.1-7(a) for final detection and subsequent spectrum estimation. Dispersive photonic-crystal lattice, combines high resolution with small footprint; however, it has only been applied to the detection of individual spectral lines.

Another type of waveguide coupled spectrometer is based on disorder and scattering. The working principle of random spectrometers is to introduce randomly placed holes in the silicon chip to scatter incoming light. Prevented from traveling in a straight line, the light beams bounce from one hole to another, increasing the effective distance they travel to get through the chip.

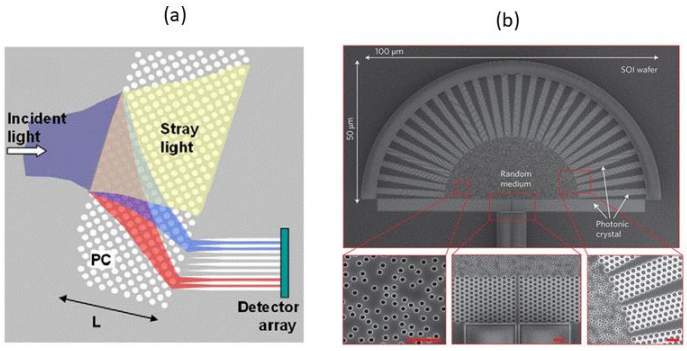

Figure 1-7:(a)PhC superprism. (b)) Disordered semicircular PhC.

The advantage of utilizing multiple scattering in a disordered medium is that it folds the optical paths, making the effective path length longer than the linear dimension of the system. In Reference[26] they designed and fabricated the random spectrometer in a silicon on- insulator (SOI) wafer. As shown in the scanning electron microscope (SEM) images in Fig.1-7(b), the two-dimensional scattering structure is a random array of air holes etched into the silicon layer. A ridge waveguide delivers the probe light to the random array, where light is scattered by the air holes and begins diffusing in all directions. The signal reaching the other end of the random structure is then detected. A spectral resolution of 0.75 nm at

a wavelength of 1,500 nm in a 25-mm-radius structure is achieved. Such a compact, high-resolution spectrometer is well suited for lab-on-a-chip spectroscopy applications

1.6 Examples of Spectrometer with Free Space Input

In free space optics, light energy is collected from open beams and surfaces and sent on to the spectrometer. Free-space coupled spectrometers offer much broader use such as imaging. The most important example is the color camera that relies on three spectral filters: Red(R), Green(G), Blue(B).

An example of free space coupled spectrometers is a colloidal quantum dot (CQD) spectrometer with a two-dimensional absorptive filter array composed of colloidal quantum dots[27].

CQDs are semiconductor nanocrystals with radii smaller than the bulk exciton Bohr radius, which leads to quantum confinement of electronic charges, with decreasing crystal size strengthening confinement and hence increasing the effective bandgap, and blue-shifting both optical absorption and fluorescent emission. Fig.1-8(a) illustrates how a basic quantum dot spectrometer operates. The measurement of an incident-light spectrum by a quantum dot spectrometer is based on the measurement of the total transmitted intensity of the spectrum that passes through a given CQD filter. This intensity measurement is repeated for each CQD filter, resulting in a set of measured transmitted-light intensities. The original (incident) light spectrum is computationally reconstructed on the basis of this set of transmitted-light intensities.

The operation of a quantum dot spectrometer can be made more efficient by measuring the set of intensities simultaneously with a collection of light detectors, each of which is coupled to a designated CQD filter (Fig.1-8b). If the collection of light detectors is arranged

into a miniaturized, two-dimensional detector array such as a charge coupled device (CCD) array detector and the set of CQD filters is integrated into a CQD filter array and coupled to the detector array, then a quantum dot spectrometer can perform spectral measurements in a snapshot fashion, without scanning or switching filters.

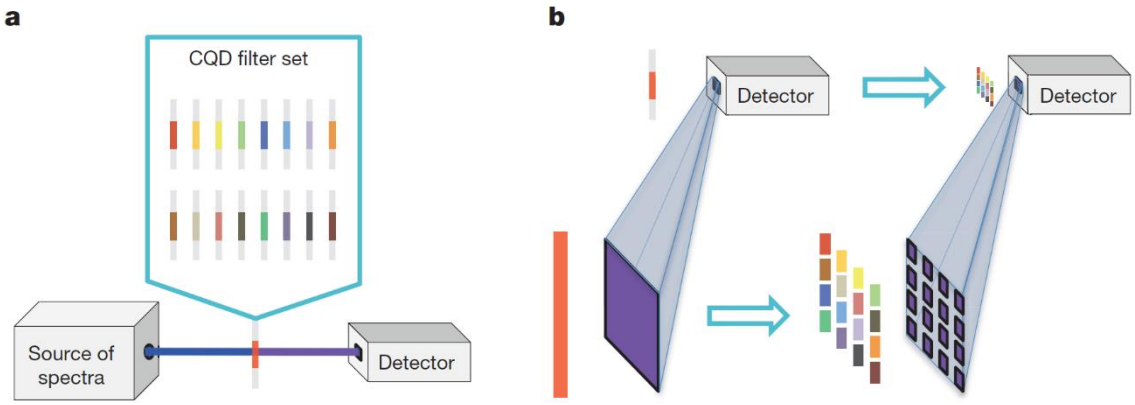

Figure 1-8:(a) A basic quantum dot spectrometer is composed of a set of CQD absorptive filters and a light detector. (b) A more efficient quantum dot spectrometer measures the set of intensities in parallel by using an array detector, with each detecting element dedicated to one CQD filter[28].

The CQD spectrometer represented in Reference[28] exploits the absorption spectrum of 195 different types of quantum dots to cover a spectral range of 300 nm (390–690 nm). The performance of the CQD spectrometer was demonstrated through its ability to measure shifts in spectral peaks as small as 1 nm.

As Fig.1-9 shows, the Colloidal quantum dot spectrometer is a broadband-filter-based spectrometer that uses CQDs as broadband filter material[27]. It means instead of measuring different bands of a spectrum individually after introducing temporal or spatial separations with gratings or interference-based narrowband filters, a colloidal quantum dot spectrometer measures a light spectrum based on the wavelength multiplexing principle: Multiple spectral bands are encoded and detected simultaneously with one filter and one detector, respectively, with the array format allowing the process to be efficiently repeated many times using different filters with different encoding so that sufficient information is

obtained to enable computational reconstruction of the target spectrum. The computational reconstruction is required since individual spectral features are not sharp enough.

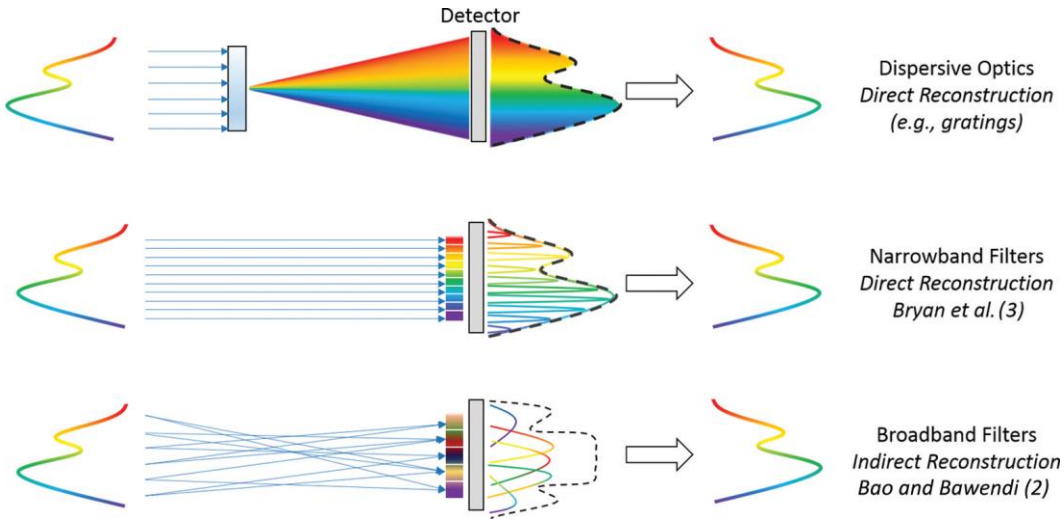

Figure 1-9: Comparison of dispersive optics, narrowband filters, and broadband filters for spectrometry[27].

Another free space coupled spectrometer is a spectrometer based on leaky-mode photonic crystal arrays[29]. It consists of a waveguide slab and a layer of photonic crystal arrays formed on the surface of the waveguide by a single lithographic or imprinting step. The photonic crystal arrays extract different wavelengths of light from the waveguide based on the matching of the crystal periods and the wavelengths, and spatially distribute the intensities.

Photonic crystal spectrometer is a direct-measurement spectrometer that uses a multielement array of photonic crystals (PCs) to create filters that operate over the UV-VIS-IR regime. In this work [29], 36-channel array is constructed with 17 elements pertaining to the visible regime and 19 additional channels responsive to the UV and IR regimes. Testing was conducted with spectra covering 450–700 nm at a resolution of approximately 20–30 nm, depending on the response function of the device.

It was shown that the presented design is theoretically able to achieve a spectral resolution of 10 nm if the channel number is increased to 50 channels, with each channel having a

response function 5 nm in width. Compared to the CQD-based spectrometer, the PC spectrometer requires substantially fewer array elements to directly calculate spectra in the visible regime. However, the minimum resolution of the CQD spectrometer is a factor of 10 lower (1 nm vs 10 nm), which can be important for sensing applications.

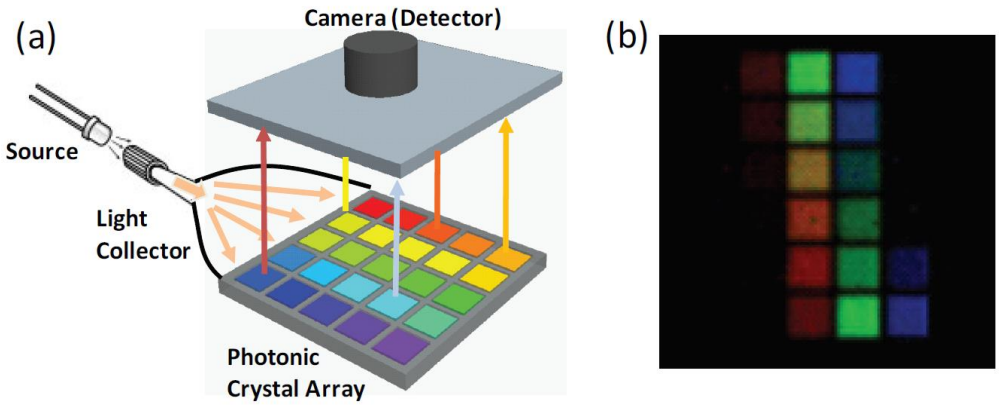

Figure 1-10: Working principle for the photonic crystal spectrometer; (b) a microscopic photo of the 17-channel photonic crystal spectrometer when illuminated with a white LED. Each square channel is 30 μm by 30 μm[29].

Recently, a scalable method to realize random spectral filters based on photonic crystals (PCs) also has been developed[17]. In contrast to quantum dots where the fabrication could be complicated by the use of non-standard complementary metal–oxide–semiconductor materials and processes, PC slabs can be defined via single exposure photolithography and only require standard CMOS materials.

A miniaturized spectrometer based on PC slabs has been proposed. PC slabs are micrometer-thin dielectric layers with periodic patterning. Light incident from free-space can couple to lateral propagation modes, where the periodic nanostructures allow light to bounce back and forth many times. The effect of path enhancement in PC slabs spreads over a broad spectral range and creates a transmission spectrum with rich spectral features. Experimentally it is shown that spectrometer based on PC slabs, operates in the wavelength

range of 550 to 750 nm with a resolution of approximately 1 nm. 36 different PC structures are used. Each PC has a size of 32 × 32 μm, and the entire spectrometer size is 210 ×210 μm as shown in Fig.1-11.

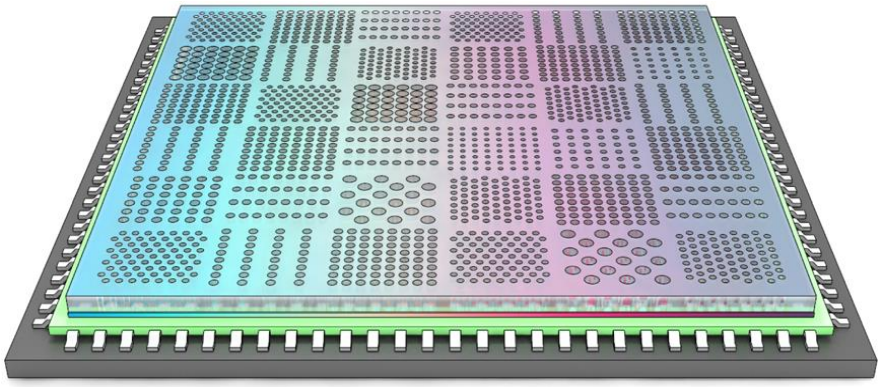

Figure 1-11:Micro-spectrometer based on photonic-crystal (PC) slabs. Schematic of the spectrometer, which consists of an array of PC slabs with different with different parameters. These slabs are integrated on top of a CMOS sensor array[17].

In this work, we demonstrate an on-chip spectrometer, readily integrable with CMOS electronics, capable of covering a wide spectral range of 400- to 1000-nm. The structure is comprised of a $SiO_2/Si_3N_4/SiO_2$ waveguide atop a silicon chip. A chirped grating is fabricated, in a single-step lithography process, on a portion of the waveguide to provide angle and wavelength dependent waveguide coupling. The spectral and angular information is encoded in the spatial dependence of the grating period. A second uniform pitch grating area provides the out-coupling to a CMOS detector array. A resolution of 0.3 nm at 628 nm is achieved without any application of signal processing deconvolution.

Table 1-2 provides some context between the various approaches that have been demonstrated. Not all of the subtleties are captured in the table, but it provides a first cut at sorting through the possibilities. Only this fully CMOS-compatible, high-volume manufacturing capable, plenoptic array has demonstrated sub-nm resolution with conventional optical lithography, with sufficient physics-based spectral resolution to avoid

the need for signal processing deconvolution.

Table 1-2:Comparison of demonstrated approaches to chip-based free space spectroscopy.

Ref.	Dispersive Element	Fab.*	Spect. Reg.†	Res. (nm)	# Pixels	Deconv. not Rqd.	CMOS Integ.
--	Chirped grating	OL	V	0.3	1150	Y	Y
[30]	Filter bank array	D	V	6	128	N	Y
[31]	Plasmonics	OL	V	3.1	17	N	Y
[32]	DBR & metasurface	EBL	NIR	2	NS	Y	N
[33]	Folded metasurface	EBL	V	1.2	80	Y	N
[34]	Waveguide and photonic xtal	EBL	V	80 nm	9	N	Y
[35]	Digital planar hologram	NIL	V	0.2	42	N	Y
[26]	2D photonic crystal	EBL	V	3 nm	25	N	Y

*OL - optical lithography; D- thin film deposition; EBL - electron beam lithography, NIL - nanoimprint lithography

† - V - visible; NIR - near-infrared (~ 1550 nm)

§ - NS - not specified

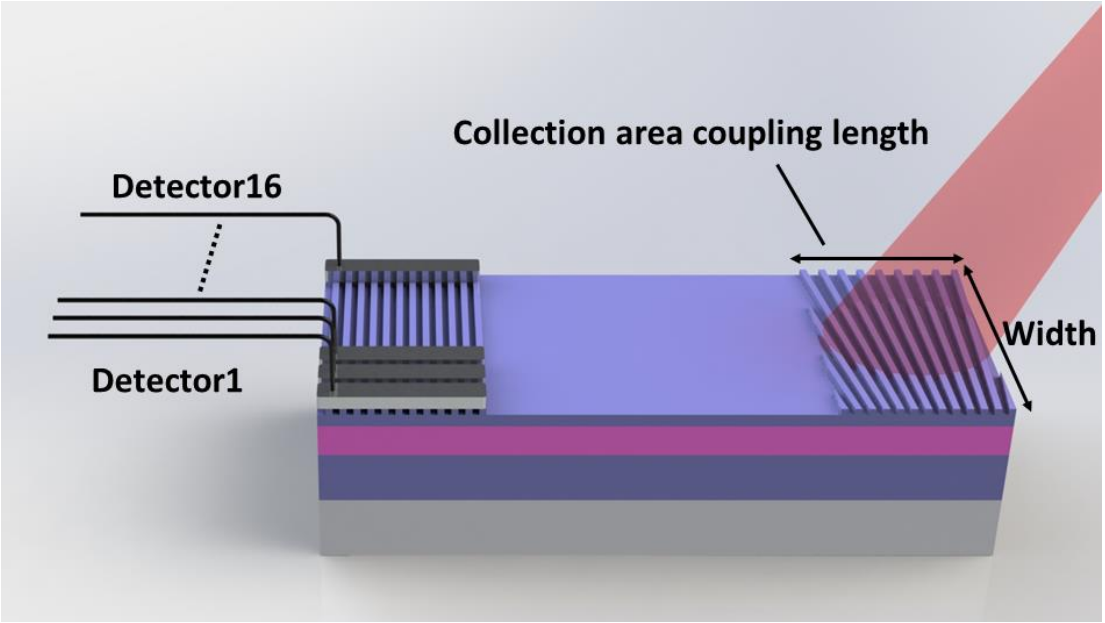

Figure 1-12: Schematic of the fixed angle chirped grating spectrometer on chip. Light is incident to the chirped grating area (chirp exaggerated for visualization) at a fixed angle of incidence, coupled into the waveguide with wavelength selectivity as a result of the grating chirp, propagated to the second grating region and out-coupled to the detector array.

1.7 Overview of Thesis

In this dissertation, we demonstrate a new structure based on waveguide coupling atop a silicon wafer using a chirped grating to provide the dispersion that leads to a high-resolution, compact, fully integrable spectrometer. Light is both analyzed and detected in a single, completely monolithic component which enables realizing a high-resolution portable spectrometer with an extremely compact footprint. Fig.1 shows the chirped grating spectrometer concept. The structure is comprised of a $SiO_2/Si_3N_4/SiO_2$ waveguide on top of a silicon wafer. Grating regions are fabricated on the top cladding of the waveguide as shown in figure1-12.

The input light is incident on a chirped grating area known as the collection area. Because of the local variation of the grating pitch across the collection area, different wavelengths of light are coupled into the waveguide at different lateral positions across the collection area. Guided light is then outcoupled through second grating region known as the detection area to the array of photodiodes placed on top of the second grating region. Therefore, spectral information is encoded in the chirped grating coupler, which is fabricated in a single lithography step, independent of the number of channels. For these initial experiments, a separate detection array was used.

The dissertation is presented in five chapters, including Chapter 1 for general introduction to spectrometers on chip. In this chapter conventional spectrometers based on dispersive element and based on Fourier transform method are presented. Also, several states of arts examples on miniaturized spectrometers are reviewed.

Chapter 2 covers the design of our fixed angle chirped grating spectrometer. Specifically, it includes slab waveguide mode solver for effective refractive indices, coupling length calculation and chirped grating period calculation as well.

Chapter 3 presents the fabrication process for chirped grating spectrometer.

Chapter 4 presents the experimental results of the chirped grating spectrometer characterization, including chirped pitch measurement, coupling length, spectral response to laser and LED sources.

Chapter 5 summarizes the research work of this project at the moment and also proposes some future work.

Chapter2

2.1 Device Design

2.2 Our Approach to Chirped Grating Spectrometer

In this work we demonstrate a new structure based on waveguide detector element[36] using a chirped grating[37] to provide the dispersion that leads to a high-resolution, compact, fully integrable spectrometer. Light is both analyzed and detected in a single, completely monolithic component which enables realizing a high-resolution portable spectrometer with an extremely compact footprint.

2.3 Waveguide Filter Element Structure

The concept of integrated waveguide spectral detection is shown schematically in Fig.2-1(a).The incident light is coupled to the waveguide at a specific wavelength and incident angle, providing a spectral/angular filtering function, and out-coupled from the waveguide downstream from the coupling region to a photodetector fabricated in the underlying silicon substrate. This structure is related to the GMR[38] filter with a detector integrated

onto the same platform as the waveguide. In this device, the gratings are of finite size, comparable to the coupling/re-radiation length, and the power coupled into the waveguide is detected as opposed to the reflection/transmission of the GMR filter. As noted below, the resolution is a function of the width of the illuminated grating along the coupling direction as well as the grating coupling strength and can be adapted to fit the resolution requirements of the application.

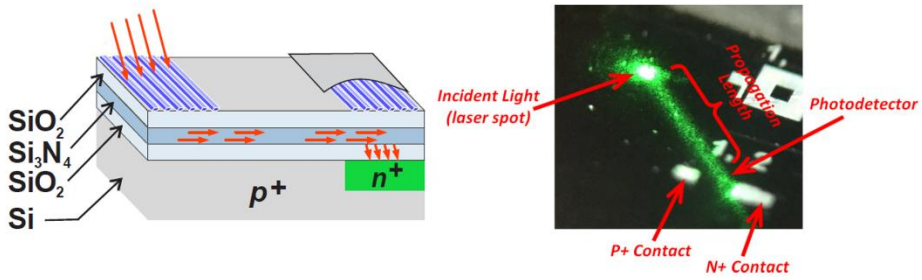

Figure 2-1:(a) Schematic of the angle-of-incidence and wavelength integrated sensor concept; (b) Demonstration of waveguide coupling and propagation for a green laser source. The grating extends across the entire device region and the light coupled from the waveguide mode to free space is observed. The cover over the detector area to eliminate direct illumination of the detector element is not yet implemented. See text for details of the waveguide and grating structure.

A visual demonstration of the propagation is shown in Fig.2-1(b) where a 532-nm laser source is used. The laser is incident on the waveguide at a position offset from the photodetector element. In this experiment, there was a grating over the entire area between the incident laser spot and the detector element, the out-coupling from the waveguide is evident as the line of scattered light leading from the laser spot to the detector element.

The grating coupler along with the single mode slab waveguide provides the necessary angular/wavelength selectivity as is evident from the coupling equation:

$$\pm k_{inc} \sin\theta_{inc} \pm 2\pi/\Lambda = k_{TE,TM}(\lambda_{inc}) \qquad (2\text{-}1)$$

where Λ is the grating period, $k_{inc} = 2\pi/\lambda_{inc}$ is the incident photon wavevector, and k_{TE}, k_{TM} are the wavelength-dependent modal wavevectors for the two polarizations.

2.4 Solution to three-layer slab waveguide structure

In the design of our waveguide filter element, there is a three layer slab waveguide on a silicon substrate. The dielectric properties of the waveguide stack are critical to the operation of the spectrometer on-chip. Therefore, it will be important to fully characterize these properties and the resulting waveguide and coupling properties of the materials and structures. For this purpose, the waveguide stack consists of a $1\mu m\, SiO_2$ as bottom cladding which was deposited through wet thermal oxidation on a Silicon wafer. The reason that we deposit such a thick bottom cladding is to eliminate leakage into silicon substrate assuring low waveguide losses. The waveguide layer is a 160 nm slab of Si_3N_4 on top of the bottom cladding. The Si_3N_4 thickness is chosen based on requirement to support only a single TE and TM waveguide mode. A waveguide mode is a transverse field distribution that propagates along the waveguide without changing shape; the solution is time-invariant. The gratings are etched 350-nm deep into the 450-nm thick top cladding. The tooth height and the initial top cladding thickness together control the coupling length.

We used MODE Solutions' FDE solver in Lumerical to carry out this slab mode analysis. Lumerical develops photonic simulation software–tools which enable product designers to understand light, and predict how it behaves within complex structures, circuits, and systems. MODE solution is a simulator within Lumerical's DEVICE Multiphysics Simulation Suite. MODE has everything we need to get the most out of our waveguide and coupler designs.

The Finite Difference Eigenmode (FDE) solver in MODE solution calculates the spatial profile and frequency dependence of modes by solving Maxwell's equations on a cross-sectional mesh of the waveguide. The solver calculates the mode field profiles, effective

index, and loss. Integrated frequency sweep makes it easy to calculate group delay, dispersion, etc. The finite difference algorithm is the current method used for meshing the waveguide geometry and has the ability to accommodate arbitrary waveguide structure. Once the structure is meshed, Maxwell's equations are then formulated into a matrix eigenvalue problem and solved using sparse matrix techniques to obtain the effective index and mode profiles of the waveguide modes. This method is based on Zhu and Brown[39], with proprietary modifications and extensions.

The MODE Eigenmode Solver uses a rectangular, Cartesian style mesh. It's important to understand that of the fundamental simulation quantities (material properties and geometrical information, electric and magnetic fields) are calculated at each mesh point. Obviously, using a smaller mesh allows for a more accurate representation of the device, but at a substantial computational cost. As the mesh becomes smaller, the simulation time and memory requirements will increase

The simulation steps for FDE solver is:

- Define waveguide structure including the waveguide and the cladding;
- Specify the materials;
- choose a mesh and accuracy;
- Choose boundary conditions;
- Specify the wavelength, or range of wavelengths.
- Maxwell’s equations are then formulated into a matrix eigenvalue problem and solved to obtain the effective index and mode profiles of the waveguide modes[40]

Fig. 2-2 shows the geometry of the multilayer dielectric slab waveguide.

This can be constructed using four contiguous rectangular structures representing the cover (SiO_2), core (Si_3N_4), bottom cladding (SiO_2) and substrate (silicon) layers.

In this section, we model the waveguide using a numerical eigenmode solver. First, the waveguide geometry is drawn using the script wg_2D_draw.lsf in listing 1 appendix A. It is then solved as a slab waveguide configuring a 1D eigenmode solver in the cross-section of the waveguide using script wg_1D_slab.lsf in listing 2 in appendix A.

The script wg_1D_slab_mode.lsf finds the effective indices of the TE1 and TM1 modes for wavelength 0.66 μm and plots the results. The first TE mode of the slab waveguide is shown in Fig.2-3. This geometry supports only TE and TM modes at 660 nm.

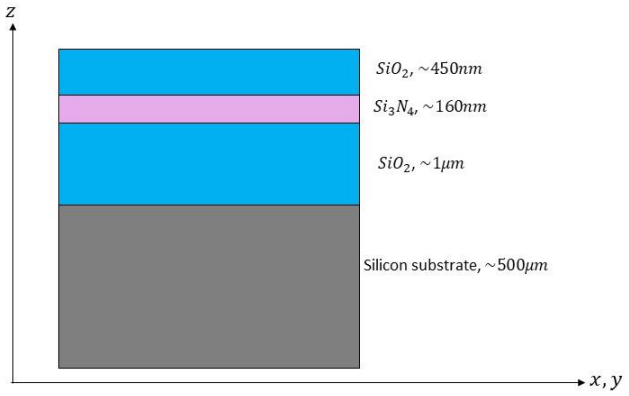

Figure 2-2 Cross-sectional view of Si_3N_4 waveguide.

The effective index is found to be $n_{eff}^{TE} = 1.756$ for the TE mode, and $n_{eff}^{TM} = 1.642$ for the TM mode. Note that this example solves the waveguide at a single wavelength. To perform wavelength sweeps, the material dispersion should be included.

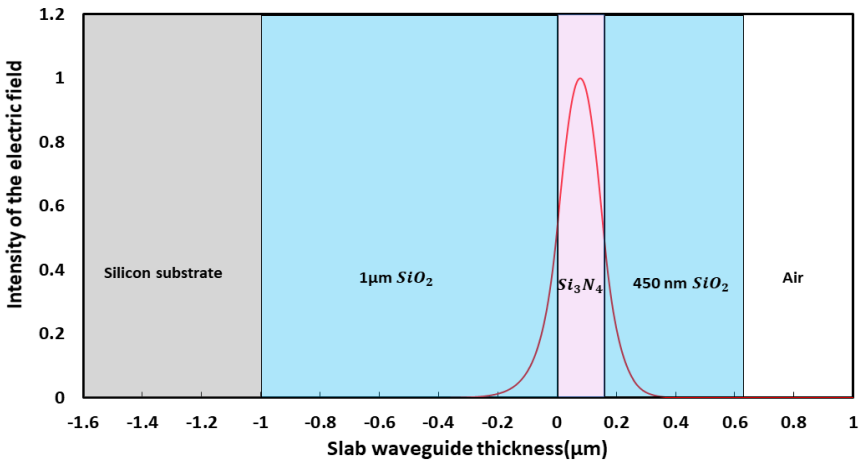

Figure 2-3: The fundamental mode profile of the slab waveguide (TE). The effective index of this mode is 1.756. Calculated using the eigenmode solver. The waveguide dimension is indicated by the pink area which is 160nm.

2.5 Waveguide Filter Element design

The waveguide filter element design involves two separated grating coupler areas. A grating coupler is a periodic structure that can diffract light from propagation in the waveguide (in plane) to free-space (out of plane). It is normally used as an I/O device to couple light between free-space and sub-micrometer waveguides. The first grating coupler region is a collection area to receive the incident light and to couple a spectral /angular selected portion of the spectrum into the waveguide and the second grating coupler region is a detection region where this spectral/angular selected spectral slice is coupled into the silicon photodetector placed on top of the second grating coupler regions.

The important characteristics of the collection region include: The spectral resolution for a fixed angle of incidence is set primarily by the smallest of the actual grating length, L_g, the dimension of the incident beam size, and the intrinsic coupling length of the grating, L_c.The resolution also depends on the angular acceptance cone of the light onto the collection area.

The coupling efficiency of the incident light with in the spectral/angular bandwidth of the grating depends on both depth/composition of the grating and the width of the collection area. For a plane wave input, the efficiency is limited by coupling of light back into the radiation field as the strength of the grating is increased.

The basic structure of the waveguide filter element is shown in Fig. 2-4.

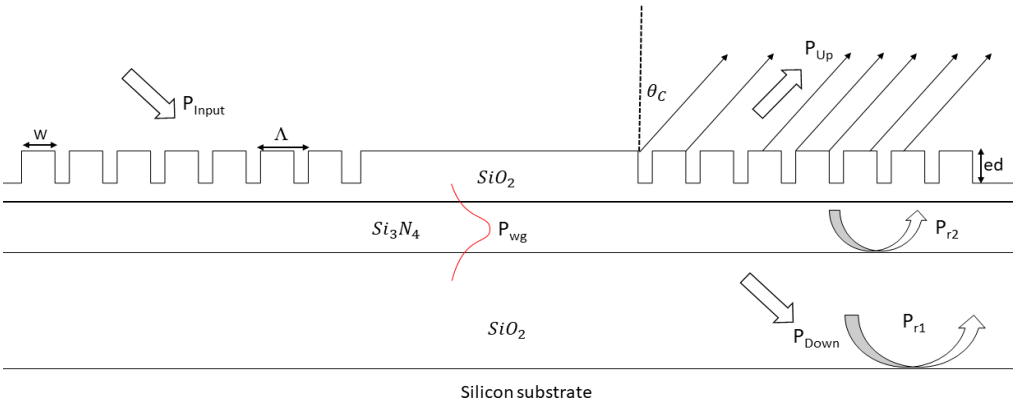

Figure 2-4: Schematic cross-section diagram of a waveguide detector element.

- The structure consists of a Silicon Nitride waveguide core, a top cladding (SiO_2), a bottom cladding (buried oxide, BOX), and a substrate (silicon).
- Λ is the period of the grating;
- W is the width of the grating teeth (assuming uniform grating);
- ff is the fill factor (or duty cycle), and is defined as ff = W/Λ;
- ed is the etch depth of the grating;
- and θ_c is the angle which couples out the light at output coupler.

$P_{wg}$is the optical power of the waveguide mode; P_{up} and P_{Down} indicate the power that goes up and the power that penetrates down into the wafer.

2.6 Performance of the Grating Coupler

The performance of the grating coupler can be described by the following parameters[41].

- Directionality: the ratio between the power diffracted upwards (P_{up}) and the input power from the waveguide (P_{wg}), which is usually expressed in decibels (dB) as $10\log10\ (P_{up}/P_{wg})$.
- Insertion loss (coupling efficiency): the ratio between the input power and the power coupled into the waveguide (P_{wg}). It is usually expressed in decibels (dB), and insertion loss can be expressed as $IL = 10\log10\ (P_{wg}/P_{input})$.
- Penetration loss: the ratio between the power lost in the substrate (P_{sub})and the input power, which is $10\log10\ (P_{Down}/P_{input})$.

There are several parameters that decide the performance of a grating coupler: period, fill factor, etch depth, incident angle, incident position, etch depth, thickness of the SiO_2 substrate, thickness of the SiO_2 cladding, number of grating periods. The thickness of the buried oxide is an important factor that have impacts on the efficiency of the grating coupler. Different reflections at various interfaces of the grating coupler is shown in Fig.2-4. Maximum coupling efficiency can be achieved when Pr_1 and Pr_2 result in constructive interference.

2.7 2D FDTD Simulation

In order to achieve the device structure with optimum operation in the wavelength range of 400- to 700-nm, we use FDTD modelling procedure using FDTD-solutions of Lumerical[42]. FDTD is a simulator within Lumerical's DEVICE Multiphysics Simulation Suite.

FDTD solves Maxwell's curl equations in non-magnetic materials:

$$\frac{\partial \vec{D}}{\partial t} = \nabla \times \vec{H} \tag{2-2}$$

$$\vec{D}(\omega) = \varepsilon_0 \varepsilon_r(\omega)\vec{E}(\omega) \tag{2-3}$$

$$\frac{\partial \vec{H}}{\partial t} = -\frac{1}{\mu_0}\nabla \times \vec{E} \tag{2-4}$$

where H, E, and D, are the magnetic, electric, and displacement fields, respectively, while $\varepsilon_r(\omega)$ is the complex relative dielectric constant $\varepsilon_r(\omega) = n^2$, where n is the refractive index.

In three dimensions, Maxwell equations have six electromagnetic field components: E_X, E_y, E_z and H_X, H_y,and H_z. If we assume that the structure is infinite in the z dimension and that the fields are independent of z, specifically that

$$\varepsilon_r(\omega, x, y, z) = \varepsilon_r(\omega, x, y) \tag{2-5}$$

$$\frac{\partial \vec{E}}{\partial z} = \frac{\partial \vec{H}}{\partial z} = 0 \tag{2-6}$$

then Maxwell's equations split into two independent sets of equations composed of three vector quantities each which can be solved in the x-y plane only. These are termed the TE (transverse electric), and TM (transverse magnetic) equations. We can solve both sets of equations with the following components:

TE: E_X, E_y, H_z

TM: H_X, H_y, E_z

For example, in the TM case, Maxwell's equations reduce to:

$$\frac{\partial D_z}{\partial t} = \frac{\partial H_y}{\partial x} - \frac{\partial H_x}{\partial y} \tag{2-7}$$

$$D_z(\omega) = \varepsilon_0 \varepsilon_r(\omega) E_Z(\omega) \tag{2-8}$$

$$\frac{\partial H_x}{\partial t} = -\frac{1}{\mu_0}\frac{\partial E_z}{\partial y} \tag{2-9}$$

$$\frac{\partial H_y}{\partial t} = \frac{1}{\mu_0}\frac{\partial E_z}{\partial x} \tag{2-10}$$

The FDTD method solves these equations on a discrete spatial and temporal grid. Each field component is solved at a slightly different location within the grid cell (Yee cell), as shown in Fig.2-5.

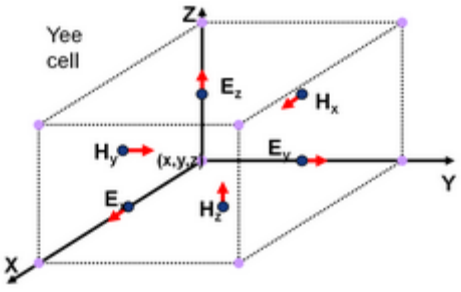

Figure 2-5: Illustration of a standard Cartesian Yee cell used for FDTD, about which electric and magnetic field vector components are distributed.

By default, data collected from the FDTD solver is automatically interpolated to the origin of each grid point, so the end user does not have to deal with this issue in their analysis.

The FDTD solver supports a range of boundary conditions, such as PML, periodic, and Bloch. The FDTD solver supports a number of different types of sources such as point dipoles, beams, plane waves, a total-field scattered-field (TFSF) source, a guided-mode source for integrated optical components, and an imported source to interface with external photonic design softwares.

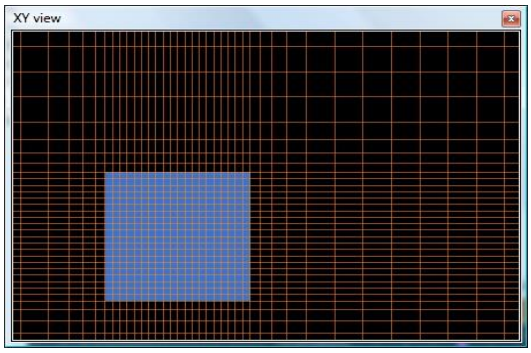

Figure 2-6: Cartesian style mesh in FDTD Simulator.

FDTD uses a rectangular, Cartesian style mesh, like the one shown in the Fig.2-6. It's important to understand that of the fundamental simulation quantities (material properties and geometrical information, electric and magnetic fields) are calculated at each mesh point. Obviously, using a smaller mesh allows for a more accurate representation of the device, but at a substantial cost. As the mesh becomes smaller, the simulation time and memory requirements will increase. The FDTD solver provides a number of features,

including the conformal mesh algorithm, that allow you to obtain accurate results, even when using a relatively coarse mesh. By default, the simulation mesh is automatically generated. To maintain accuracy, the meshing algorithm will create a smaller mesh in high index regions (to maintain a constant number of mesh points per wavelength) and highly absorbing (resolve penetration depths) materials. In some cases, it is also necessary to

manually add additional meshing constraints. Usually, this involves forcing the mesh to be smaller near complex structures (often metal) where the fields are changing very rapidly.

The electric and magnetic fields are recorded on the finite-difference mesh, as shown in Fig.2-7 for a 2D monitor, where the grey dots represent the positions where the fields are recorded.

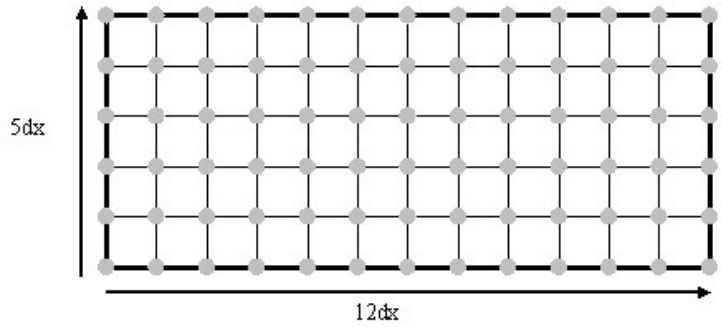

Figure 2-7: The electric and magnetic fields are recorded on the finite-difference mesh, where the grey dots represent the positions where the fields are recorded.

2.7.1 Material Characterization Using Ellipsometry

The first step using FDTD solution to design our structure, is to define the optical properties of all materials. we should make sure to account material dispersion. In order to account material dispersion, all thin film layers in the waveguide stack, are optically characterized using ellipsometry method. Ellipsometry is an optical reflectance measurement for thin film characterization. Ellipsometry can provide information on thin film parameters such as its thickness, composition and porosity. Ellipsometry measures a change in polarization as light reflects or transmits from a material structure. The measured signal is the change in polarization as the incident radiation interacts with the material. The polarization change is quantified by the amplitude ratio, Ψ, and the phase difference, Δ.

In ellipsometry, Electromagnetic radiation is emitted by a light source and linearly polarized by a polarizer. It can pass through an optional compensator and falls onto the sample. After reflection the radiation passes a compensator and a second polarizer, which is called an analyzer, and falls into the detector. The incident and the reflected beam span the plane of incidence. Light which is polarized parallel to this plane is named p-polarized. A polarization direction perpendicular is called s-polarized, accordingly. Ellipsometry measures the complex reflectance ratio ρ of a system, which may be parametrized by the amplitude component Ψ and the phase difference Δ.

The polarization of the light incident upon the sample may be decomposed into an *s* and a p component The amplitudes of the s and *p* components, after reflection and normalized to their initial value, are denoted by r_s and r_p respectively. Ellipsometry measures the complex reflectance ratio ρ, which is the ratio of r_p over r_s:

$$\rho = \frac{r_p}{r_s} = \tan\Psi . e^{i\Delta} \qquad (2\text{-}11)$$

Thus, $\tan\Psi$ is the amplitude ratio upon reflection, and Δ is the phase shift difference. Ellipsometry is an indirect method. It means that the measured Ψ and Δ cannot be converted directly into the optical constants of the sample. Normally, a model analysis must be performed. This is one weakness of ellipsometry.

Table 2-1 shows the optical properties of our waveguide structure, which is measured by ellipsometry.

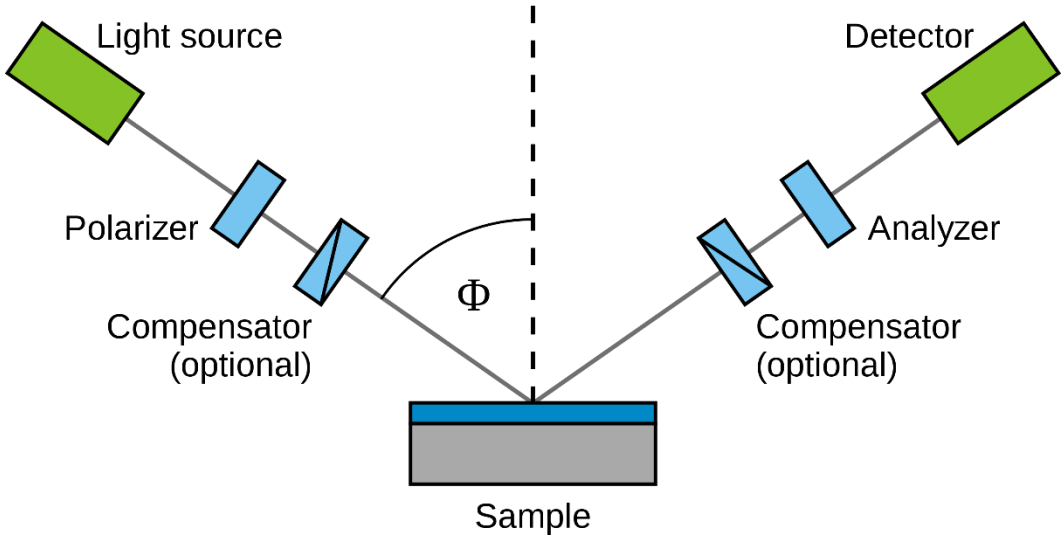

Figure 2-8: schematic set up of an ellipsometry experiment.

Table 2-1: Optical properties of the waveguide layers

Waveguide Layer	Thickness(nm)	Refractive Index, n(λ=660nm)
SiO_2(Top cladding)	450	1.45
Si_3N_4(waveguide layer)	160	2.014
SiO_2(Bottom cladding)	1000	1.46

2.7.2 Waveguide Filter Structure Design Using FDTD

After material characterization using ellipsometry, experimental material data is imported into the material database of the FDTD-solutions software. The structure is drawn, via a GUI or script. This includes defining the geometries for the silicon substrate, oxide claddings, Nitride waveguide and grating couplers. Next, simulation volume is defined. The simulation volume needs to be smaller than the structure to be simulated, i.e. the input and output grating couplers are extended past the simulation boundaries. The mesh can be

defined by the number of mesh points per wavelength in the material. We usually use large mesh size for first time simulations to check if the simulation is right. Later, we use small mesh size for more accurate simulation results. In FDTD, we have the option of using conformal meshing. This automatically generates a graded mesh which has more accurate steps at the interfaces, curves, slots and small features. However, relatively larger mesh sizes will be used for the rest of the simulation domain. Next, the boundary conditions are defined. Perfect Matching Layers (PML) are the most general ones, which are used to absorb all the light leaving the simulation. PML absorbing boundary conditions are impedance matched to the simulation region and its materials. This allows them to absorb light waves (both propagating and evanescent) with no reflections. An ideal PML boundary produces zero reflections, however, in practice, there will always be small reflections due to the discretization of the underlying PML equations. Next step is to define simulation time. In our structure which consists of a pair of grating couplers, the light is expected to pass through once so simulation time is typically estimated by $t = L/v_g$, where L is the propagation length, and $v_g = c/n_g$ is the group velocity and is determined by the waveguide's group index,n_g, found via mode calculations. The next step is to add a Gaussian source. Gaussian source defines a beam of electromagnetic radiation propagating in a specific direction, with the amplitude defined by a Gaussian cross-section of a given width. By default, the Gaussian sources use a scalar beam approximation for the electric field which is valid as long as the waist beam diameter is much larger than the diffraction limit. The scalar approximation assumes that the fields in the direction of propagation are zero. Then, we should add monitors. Monitors are used to measure the optical field quantities, both E and H, at the chosen locations. Since FDTD simulations are in the time

domain, the fundamental monitor is the time-domain monitor. However, it is useful to calculate the frequency response of the device, and to normalize this response relative to the launched power spectral density. The result is a frequency-domain field profile monitor. This monitor can plot the field profile or generate the optical transmission spectrum of the device.

Fig.2-9 shows the simulated structure with added source and monitors for waveguide detector element. Parameter sweeping is typically performed when designing devices. Parameter sweeps are useful for finding the optimum value of a parameter, and for studying the sensitivity of the design performance to certain parameters or running a series of simulations with a set of varying parameters.

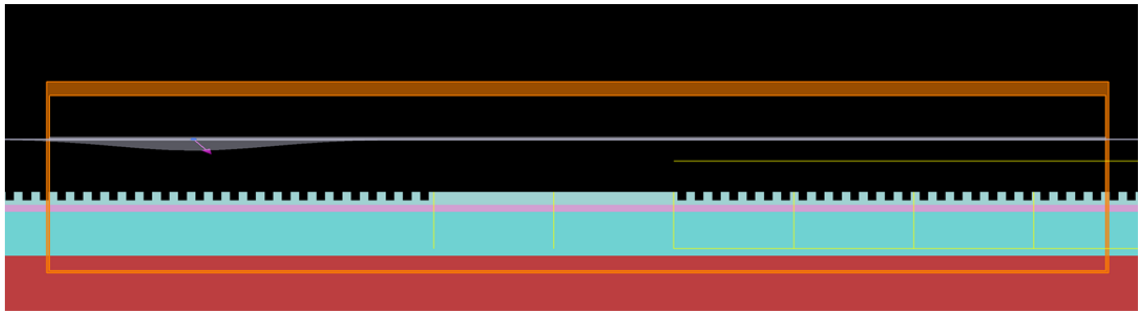

Figure 2-9: 2D FDTD simulation configuration for the waveguide filter structure, including the optical source. optical source is used to inject light into the simulation from the free space region. Power monitors are used to measure the power in the waveguide and power outcoupled to free space region and silicon wafer at the second grating coupler.

2.8 Design Parameters

The file grating_coupler_2D_startdesign.fsp in listing 3 in appendix A contains a waveguide filter structure consisting of two grating coupler structures and nitride waveguide structure with a 160 nm thick nitride layer a, 450 nm thick oxide top cladding and 1 µm thick buried oxide layer. The grating has a period of 380 nm, an etch depth of 350 nm and a duty cycle of 0.5.

The first grating coupler is used to launch light from free space into the waveguide. The second grating coupler couples out the coupled guided mode to the free space. The transmitted power exiting the top of the structure can be recorded using a frequency domain field and power monitor placed just above the second grating coupler as is shown in Fig.2-9.

2.8.1 Incident Angle

The incident angle of a grating coupler is defined as the angle between the incident wave (or out-coupled wave) and the normal to the grating surface. A positive angle indicates the case in which the incident wave and the coupled wave in the waveguide propagate in the same direction and a negative angle indicates the case in which the incident wave and the coupled wave in the waveguide propagate in opposite directions.

Figure (2-10a) shows the coupling wavelength and coupling angle for a range of grating periods for the following waveguide structure. The waveguide structure consists of a SiO_2 (n_{SiO_2}~1.5) lower cladding with a thickness of 1 μm to eliminate leakage into the silicon substrate assuring low waveguide losses. The Si_3N_4 guiding layer was~200 nm thick ($n_{Si_3N_4}$~1.8) and the top cladding was SiO_2 (n_{SiO_2}~1.43) with a thickness of ~30 nm. For the longer period gratings, multiple orders are included as indicated (e.g. 800/2 refers to the second-order of a 800 nm pitch grating, etc.). Figure (2-10b) shows the required grating periods for a fixed angle of incidence[36].

In the case of chirped grating spectrometer, it will be important to sample the spectrum as a function of wavelength at a fixed angle of illumination. For example, at the fixed angle of $\theta_c = 30^{\circ}$ illumination the required grating pitch varies from 330- to170-nm for backward

coupling and from 600- to 325-nm for forward coupling according to figure 2-10b. So, our grating needs to have a 275 nm chirp range for forward coupling and a 160 nm chirp range for backward coupling to sample the spectrum across the visible range.

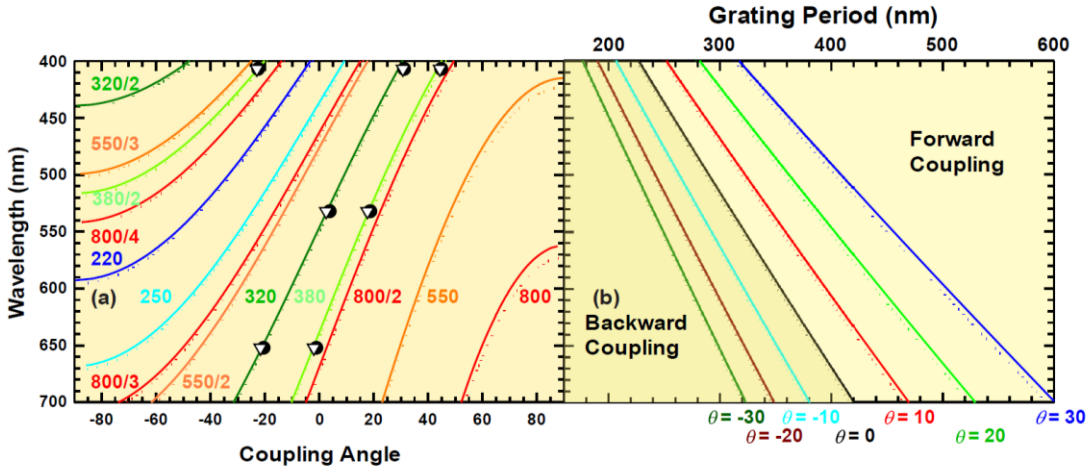

Figure 2-10: a, Wavelength vs. coupling angle for different grating periods. Multiple orders of the grating are shown. (e.g. the notation 800/2 refers the second order of a 800 nm pitch grating). b, Wavelength vs. grating period at a fixed angle(periods are indicated at the top of the figure, the fixed angles are indicated at the bottom of the figure. Both forward and backward scattering regimes are indicated. For both figures the solid lines are TE modes and the dotted lines are the TM modes.

2.8.2 Coupling Strength

The coupling strength is an important parameter since the goal is to maximize the power coupled into the waveguide. Considering only a single waveguide mode and the incident and transmitted/reflected fields, the intensity of the modal output relative to the input plane wave intensity for grating coupling is given by

$$\frac{I_{mode}}{I_{in}} = \left(\frac{\eta}{\alpha}\right)(1 - e^{-\alpha L})^2 \qquad (2\text{-}12)$$

where η is a coupling constant, α is the inverse coupling length (both defined in [44]) and L is the width of the coupling region. For weak coupling the modal intensity scales as (L^2) while it saturates for strong coupling as a result of re-radiation back into the reflected/transmitted farfield plane waves. The coupling linewidth is proportional to L^{-1},

so for a broadband source(e.g. an LED) the power in the mode scales as $\frac{\left(\frac{\eta}{\alpha}\right)\left(1-e^{-\alpha L}\right)^2}{L} \approx \eta\alpha L$ for weak coupling[36].

2.8.3 Bottom Cladding Thickness

In order to achieve the structure optimally operated in the wavelength range of the 400- to700-nm, the thickness of the buried oxide should be chosen to achieve constructive interference between Pr_1 and Pr_2, therefore, low insertion loss can be obtained for the range of the wavelength 400- to 700-nm. In order to choose the right buried oxide thickness, we run "buried oxide thickness" in the Optimization and Sweeps script in listing 4 in appendix A from 1um to 4.5 um for two wavelengths of 400-nm and 700-nm.

Simulation results for varied buried oxide are shown in Fig.2-11 from 1 μm to 4.5 μm for two wavelengths of 400 nm and 700 nm.

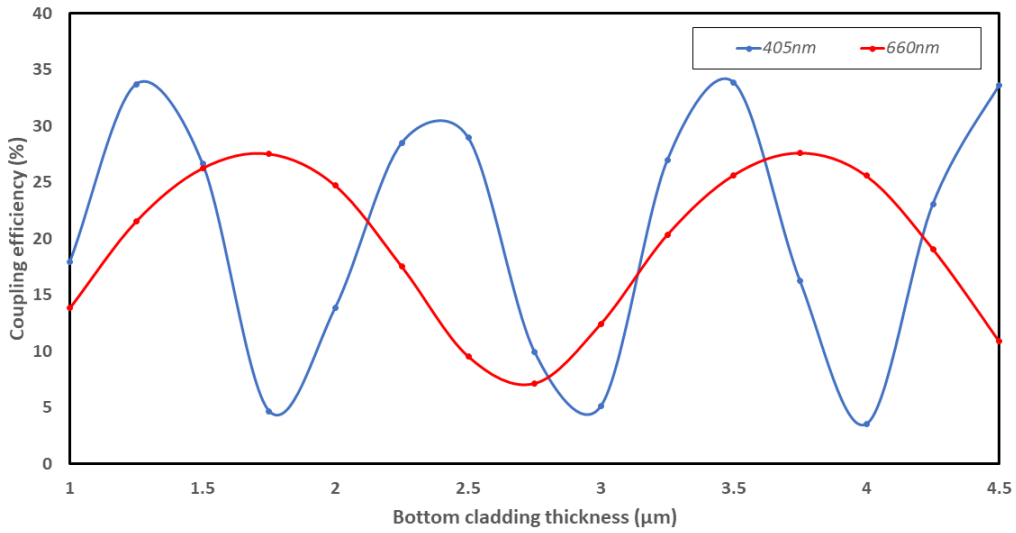

Figure 2-11: Coupling efficiency vs bottom cladding thickness

The coupling efficiency of the grating coupler oscillates in a sinusoidal manner, which is determined by the interference between Pr_3 and Pr_2.

The thickness of the buried oxide for our waveguide detection element is chosen to be 1μm. The bottom oxide serves several functions: 1) it is thick enough so that the waveguide mode does not penetrate to the silicon, resulting in low loss propagation of the waveguide mode; 2) the SiO_2/Si interface reflects a portion of any incident light transmitted by the grating back up towards the grating, the path length can be adjusted for constructive interference between the light coupled into the waveguide in the forward and backward paths at a specific wavelength/incident angle range.

2.8.4 Coupling Length

One of the key components in the design of the chirped grating spectrometer is the size of the grating coupler regions. For a sufficiently long coupling area, the coupling efficiency is limited by coupling of the light back into the radiation field. The optimum coupling efficiency occurs for a coupling length matched to the physical length of the grating.

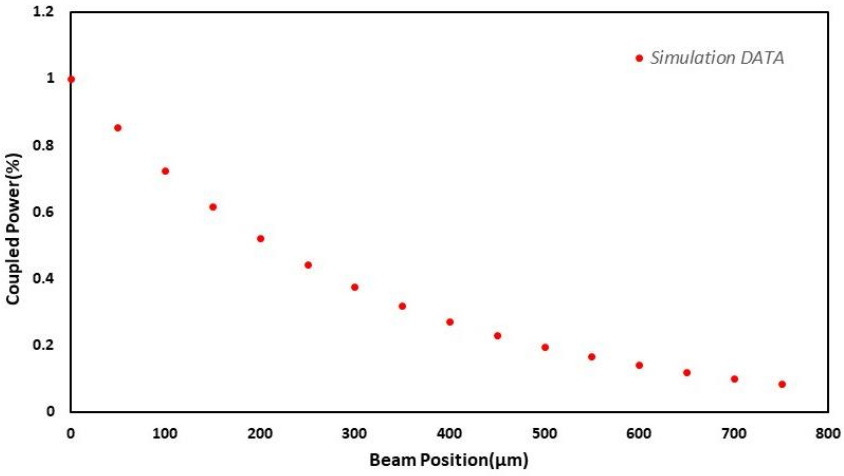

Figure 2-12: Coupled power versus beam position sweep at resonant angle. As the distance between center of Gaussian beam(λ = 621 nm, TE polarized)focused to the 100 μm diameter spot and the end of the grating coupler (beginning of the propagation region) increases, the transmitted power to the detection area decreases due to reradiation of the coupled power back into free space.

Coupling length is found by source position sweep at resonant angle simulation. The test grating coupler pitch is 380 nm and the grating is etched 360 nm into the 450 nm thick SiO_2 top cladding. In order to design a device with optimum grating coupler size, we run "Beam position" sweep at resonant angle to find the coupling length for $\lambda = 621$ nm. As the distance between center of input laser beam ($\lambda = 621$ nm) and the edge of the grating coupler increases, the transmitted power to the detection area decreases due to reradiation of the coupled power back into free space. The power attenuation coefficient$\left(\alpha = \frac{1}{L_c}\right)$[45] or equivalently the grating coupling length is calculated to be $L_c = 305\ \mu m$ for TE polarization using Lumerical FDTD Solver[46] Therefore, the optimized collection region length should be about $L_c = 305\ \mu m$ to achieve optimum coupling efficiency.

2.9 Derivation of Resolution Limits

The resolution of the grating coupler is set by the smallest of the coupling length, L_C; the width of the source illumination at the grating; or the physical width of the grating. In the current experiments, the L_C of ~ 300 μm dominates. The resonance condition is $\Delta k(\theta, \lambda, d, j) = 0$ and the resonance linewidth is given by $\Delta k(\theta \pm \delta\theta/2, \lambda \pm \delta\lambda/2, d \pm \delta d/2, j) = \pm\pi/L_C$.

Using coupling equation in (2-1), we can write phase matching condition:

$$\Delta k(\theta, \lambda, d, j) = \frac{2\pi}{\lambda}\sin\theta + j\frac{2\pi}{d} - \frac{2\pi}{\lambda}n_{eff}(\lambda) \qquad (2\text{-}13)$$

As we know, at resonant angle:

$$\Delta k = 0, \frac{2\pi}{\lambda}\sin\theta + \frac{2\pi}{d} - \frac{2\pi}{\lambda}n_{eff}(\lambda) = 0 \qquad (2\text{-}14)$$

If we take the full width half maximum at $\Delta k(\xi)L_C = \pi$ where ξ is one of the independent variables, we can calculate angular resolution:

$$(\delta\theta)_{FWHM} \sim \frac{\lambda}{2L_C \cos\theta} \tag{2-15}$$

Wavelength resolution:

$$\delta\lambda \sim \frac{\lambda d}{2L_C\left(1 - d\frac{\partial n}{\partial \lambda}\right)} \tag{2-16}$$

And grating period variation:

$$\delta d \sim \frac{d^2}{2L_C} \tag{2-17}$$

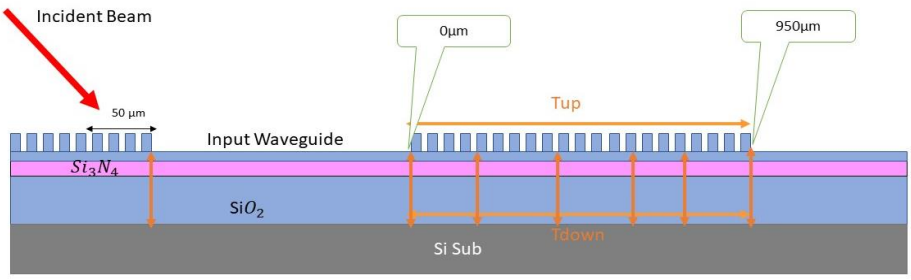

Figure 2-13: 2D FDTD simulation configuration for the waveguide filter structure, including the optical source. optical source is used to inject light into the simulation from the free space region. Power monitors are used to measure the power in the waveguide and power outcoupled to free space region and silicon wafer at the second grating coupler.

Using FDTD-Solutions in Lumerical, we simulate the waveguide structure element as shown in Fig.2-13 to calculate the Angular resolution of the device $\Delta\theta$. The input coupler length is 450 µm. The input waveguide length is 100 µm. The output coupler length is 950 µm. we insert power monitors at different positions of the output coupler to see how much power left into the waveguide. T_{up} is the power monitor which shows how much power couples out into the air and T_{Down} is the power monitor which shows how much power couples out to the substrate. Light with $\lambda = 621$ nm and beam radius of $\omega_0 = 500$ µm

incident on the input grating coupler at a position 50 µm away from the edge of the coupler and input waveguide as shown with red arrow in the Fig.2-13. When we sweep the angle of illumination, as it is shown in Fig.2-14, from the power recorded in the T_{up} monitor we can see the incident light couples into the waveguide at the coupling angle of $\theta_c = 8.05°$ and $(\delta\theta)_{FWHM} \sim 0.06°$ from simulation result.

If the light incident at coupling angle, $\theta_c = 8.05°$ and we record the power left inside the waveguide at different position of the output grating coupler we can calculate that coupling length is $L_c = 305$ nm as shown in Fig.2-15.

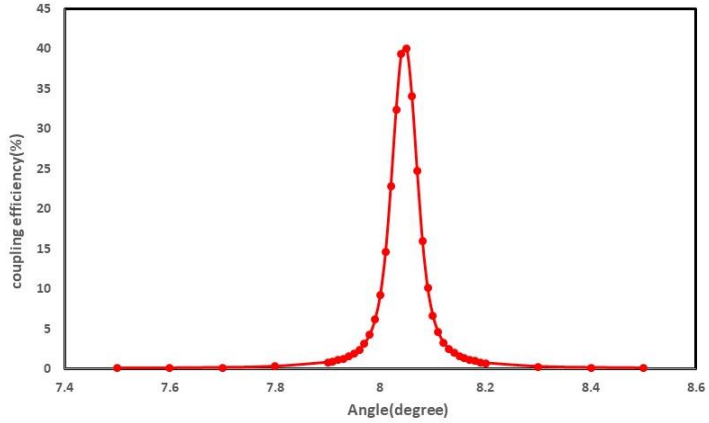

Figure 2-14: Angular sweep of the beam. As the incident angle is scanned, the coupled power is recorded inside monitors T_{up} and T_{Down}.

From experiments, at a wavelength of 632.8 nm for an L_C of ~ 300 µm, using equation (2-15) gives: $(\delta\theta)_{FWHM} \sim 0.057°$ which is in a good agreement with simulation result. If we assume $n_{eff}^{TE} = 1.75076$ at λ=623 nm and $n_{eff}^{TE} = 1.75035$ at λ=633 nm, then, $\frac{\partial n}{\partial \lambda} \sim 0.00041\ nm^{-1}$. Using equation 2-16 and 2-17 and d=505 nm, we can calculate $\delta\lambda = 0.37$ nm and $\delta d = 0.33$ nm.

The above numbers show that grating coupling provide us a high resolution chirped - grating spectrometer on chip.

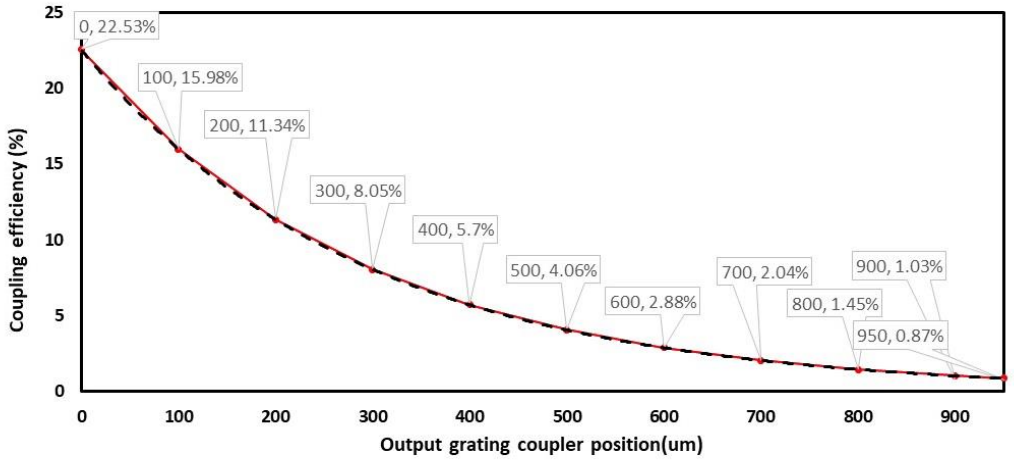

Figure 2-15:The coupled power is recorded at different positions of the output grating coupler.

2.10 Experimental Results for Waveguide Filtered Element

For initial testing of the waveguide filtered CMOS compatible photodetector, diode-based, multi-mode RGB lasers of wavelengths 652.3-, 532.2- and 407.8-nm were used. The experimental setup consists of the laser light source followed by an infrared filter, polarizer, long focal length lens and an aperture to provide uniform illumination across $the \sim 200 \times 200\ \mu m^2$ coupling region.

Incoming light at the resonant wavelength and angle is scattered by the grating and couples into the waveguide, propagates to the junction area, and is decoupled into the photodetector. Out-of-resonance light does not couple into the waveguide and is either reflected or transmitted into and absorbed in the silicon far from the photodetector active area and does not contribute to the photocurrent. The illumination angle of the incident beam relative to the grating was scanned with a resolution of 6 arcsec. Fig.2-17 shows the

ratio of the measured photocurrent to the incident power of each laser source, normalized in each case to the peak measured photocurrent, for two sets of measurements with the same waveguide structure but different grating pitches of 320- and 380-nm. The results for

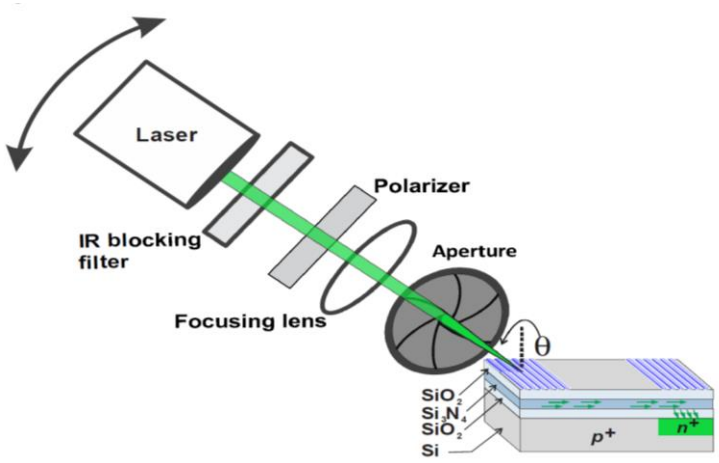

Figure 2-16: Experimental arrangement. All of the optical components are mounted on a computer controlled arm that rotates about the top grating on the waveguide at a position offset from the photodetector junction. Contacts are etched and metalized on the top surface of the silicon wafer and probes are used in these initial experiments.

the two pitches are vertically offset for clarity. The measured angular linewidths [< 0.5° corresponding to a wavelength spread of ~3 nm ($\Delta\lambda \approx -d \cos\theta \, \Delta\theta$) from equation 2-1 are slightly wider than the theoretical predictions (discussed below) and show some fine structure, probably corresponding to the multi-mode character of the lasers. The linewidth is a convolution of the scattering/absorption propagation losses of the bare (no grating) waveguide and the spectral width corresponding to the length of the coupling area (the smallest of the width of the grating, the illumination spot size, or the coupling length). In these experiments, the laser spot size(~200 μm) along with the intrinsic bandwidth of the multimode laser sources are the dominant contributions to the observed linewidth.

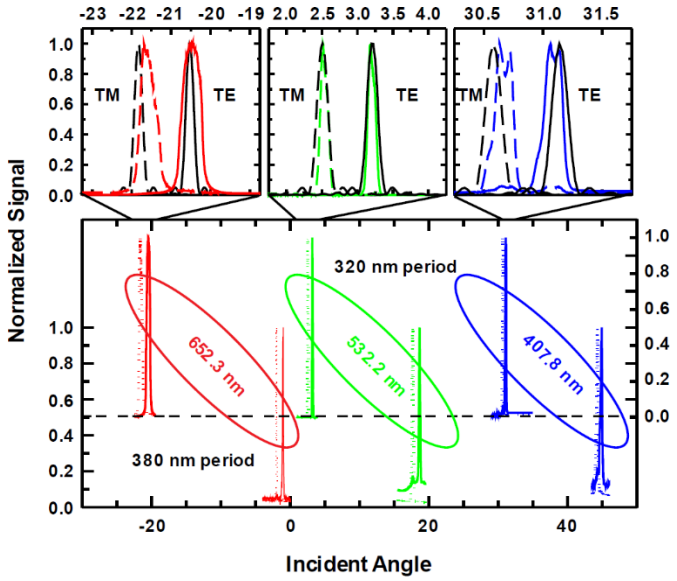

Figure 2-17: Angular resolution of a grating coupled waveguide detector for RGB laser sources. The expanded views show the TE (solid) and TM (dotted) experiments and simulations (black lines).The bottom panel shows the results with the same waveguide with grating periods of 320- and 380-nm. The 320-nm grating results are offset and expanded in the top panels and compared with simulation.

Chapter3

3.1 Fabrication

The fabrication of chirped grating spectrometer follows very standard microelectronic fabrication procedures and includes four major steps.

1. **Waveguide Fabrication** using thin film deposition methods[47], a three-layer slab waveguide is fabricated. For these experiments all three layers were fabricated by a commercial fabricator.
2. **Uniform Grating Patterning with IL** Using Interferometric lithography[48], uniform grating is patterned into the pre-coated photoresist (PR)layer on top of the 16×10 mm die.
3. **Chirped Grating Patterning with IL** Using Interferometric lithography, hyperbolically chirped grating is patterned into the pre-coated photoresist (PR)layer on top of the 16×10 mm die.
4. **Grating Pattern Transfer with Dry Etch** Using inductively coupled plasma (ICP)[49], chirped grating pattern is transferred into the top clad of the slab waveguide structure on the die.

3.2 Waveguide Fabrication

3.2.1 Bottom Cladding (SiO_2)Deposition

Wet oxidation[50] is used for growth of 1μm SiO_2 films on 100 mm (4- inch)$< 100 >$ orientation Si wafers of thickness 525 ± 25 μm. Wet thermal oxide films are generally for applications where a thicker silicon dioxide layer is necessary. To prevent impurities, these films usually grow in quartz tubes using a combination of heat and pure steam. During the oxidation process, the temperature in the external heater is raised to more than 800°C. This causes the gases to spontaneously ignite and produce a blue flame without an ignition source. The flame creates pure steam, hence the name *wet* thermal oxide. The pure steam moves through the tube that houses the flame into the furnace where the wafers are. Once the steam enters the quartz chamber, it expands and evenly distributes throughout the furnace.

The wafers, which either stand horizontally or stack vertically, are in the furnace for several hours, as time varies depending on the target film thickness. The growth of SiO_2 is not linear, so when a wafer is in a 1000 °C furnace for 5 hours, an oxide layer of approximately 1000 nm will form; and if that same wafer remains in the furnace for 24 hours, the layer of 2500 nm will form[51]. The second wafer was in the furnace for nearly five times longer, but the oxide layer is only about twice as thick. This is because as the oxide layer grows, it becomes more difficult for oxygen to penetrate the oxide layer and interact with the silicon substrate to create SiO_2.

3.2.2 Waveguide Layer (Si_3N_4) Fabrication

160 nm Si_3N_4 is deposited on top of the 1μm SiO_2 using a Low pressure chemical vapor deposition (LPCVD) process[52]. Low pressure chemical vapor deposition is a process that

uses heat to initiate a reaction of a precursor gas on a substrate. It is performed at low pressure to decrease unwanted gas phase reactions with the surface of the wafer and the result of this process is high uniformity wafers that are easy to reproduce. LPCVD nitride is performed in a quartz tube reactor and undergoes a standard chemical vapor deposition process, performed in a vacuum. After loading the wafers into the reactor, the tube is evacuated to a low pressure between 10 mTorr and 1 Torr, depending on the wafer size. Once the wafers are under vacuum, the furnace heats up. The temperature inside the system can vary between 425°C and 900°C, depending on the temperature needed for the precursor gas to begin to decompose[53]. After reaching the correct temperature, the system releases gas into the tube to react with the wafers and create a film on the substrate surface. Once the wafers have the correct film thickness and density, excess gas is pumped out of the system and the furnace is moved back to standard room pressure and temperature. Silicon nitride is a well-known dielectric material that is transparent in the visible-NIR and beyond, compatible with CMOS based processes for low-cost mass fabrication, possesses relatively high refractive index (n =2.0) for tighter confinement. The Si_3N_4 thickness in our structure is chosen based on requirement to support only a single TE and TM waveguide mode.

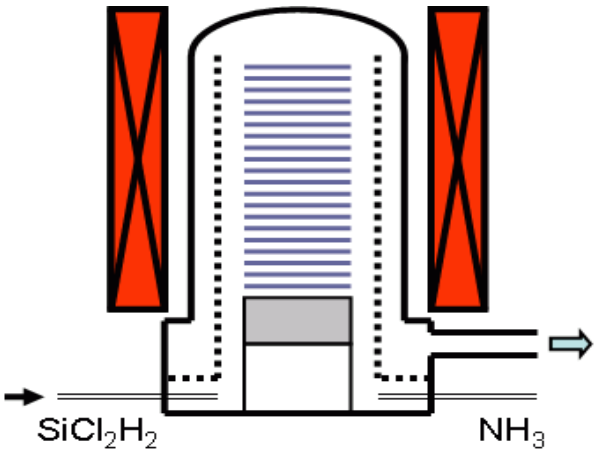

Figure 3-1: Simplified view of the employed LPCVD system[53].

3.2.3 Top Cladding (SiO_2) Fabrication

450 nm SiO_2 is deposited on top of the 160 nm Si_3N_4 using a Plasma-enhanced chemical vapor deposition (PECVD) process[54]. PECVD is a low-temperature process (200–400 C) that enables stress-free thick-film deposition.

In a PECVD system, reactant gases flow into process chamber through a shower head which is a large perforated metal plate located above the sample. The shower head helps to provide a more uniform distribution of reactant gas flow over the sample surface. An RF potential is applied to the shower head to generate a plasma. Energetic electrons in the plasma ionize or dissociate reactant gases to generate more chemically reactive radicals[55]. These radicals react to form the thin film of deposition material on top of the sample. The energy supplied by plasma provides the key advantage of reduced process temperatures for PECVD compared to LPCVD where all of the energy for reaction is supplied thermally.

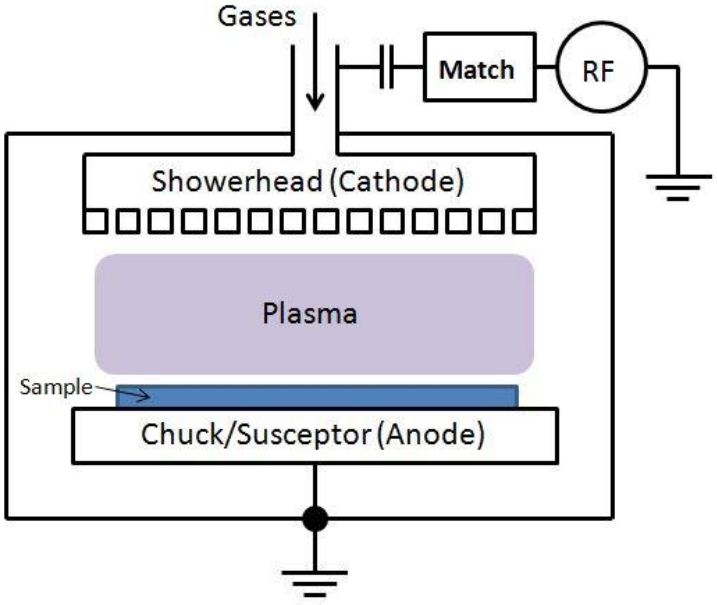

Figure 3-2: PECVD chamber diagram[55].

Following baseline recipe was used for film deposition after loading the wafer into the chamber via loadlock.

Step 1: System chamber is pumped below 5mT base pressure for 1 minute with electrode temperature at 350 °C.

Step 2: Chamber is pre-heated and purged with N_2 having flow rate of 700 SCCM at pressure set point of 1400 mT and electrode temperature at 350 °C for 1 minute (for 4-inch wafer).

Step 3: SiO_2 is deposited in this step with following precursors and chamber conditions:

- Silane (10 % SiH_4 in Helium) flow rate: 265 SCCM
- Nitrous Oxide (N_2O) flow rate: 1000 SCCM
- Nitrogen (N_2) flow rate: 500 SCCM
- Pressure: 1800 mT
- High frequency RF power: 140 W
- Electrode temperature: 350 °C

Step 4: Chamber is pumped to base pressure and wafer removed from loadlock.

3.2.4 Die Cleaning

The wafer with the waveguide layer stack is sequentially rinsed with acetone, methanol, and isopropanol for 10 to 15 seconds, then followed by a DI water rinse for about 10 seconds. Immediately afterwards, die is blown dry with N_2 gas. Then it is baked in contact

mode, at 200℃ on hot plate for about 5 minutes for dehydration. After that, die is cooled down to room temperature for spin coating.

3.3 Uniform Grating Patterning with IL

3.3.1 ARC Coating

An anti-reflection coating (ARC) is required to avoid a standing wave pattern on the side walls of the grating patterned in photoresist (PR) and it helps PR adhesion as well. ARC has a complex refractive index and is absorptive at the IL wavelength. The mechanism that ARC works is based on processes of light absorption in it and also the destructive interference between the light reflected from the PR/ARC interface and the light transmitted back into PR layer through that interface from the ARC interface. With given substrate and PR and ARC, the thickness of the ARC layer needs to be correct for particular IL incident angles, which is controlled in the spin coating process. With well controlled ARC thickness, only IL incident light beams interfere to make the grating pattern, without a standing wave pattern appearing on the side wall of the PR pattern. The target thickness of ARC is calculated with our MathCAD program to be ~70 nm, then spin coat RPM is looked up from the spin coat speed curve in the ARC data sheet, as shown in the following table. ARC spin coat recipe is shown in table 3-1.

Table 3-1: Recipe for anti-reflection coat (ARC) spin coating.

ARC Model	Icon-7
Spin Coating Speed(rpm)	3000
Soft Bake Temperature (℃)	180
Soft Bake Time(s)	60
ARC Thickness(nm)	70

3.3.2 PR Coating

Spin coat of PR is very similar to that for ARC and is done right after ARC coating. To determine the thickness of the PR layer, we used ellipsometry.

Target grating period also needs to be considered because the aspect ratio (ratio between PR line height and width of patterned grating in PR) should not be too high to cause PR pattern collapse which will affect the pattern transfer into substrate.

Based on the above considerations, NR7500P is chosen for the IL grating pattern process which gives target thickness of~500 nm at speed of 3500 rpm in spin coat. PR spin coat recipe is shown in table 3-2.

Table 3-2: Recipe for photoresist spin coating.

Photoresist	NR7500P
Spin Coating Speed(rpm)	3000
Soft Bake Temperature (℃)	150
Soft Bake Time(s)	60
PR Thickness(nm)	500

3.3.3 Uniform IL Patterning for Detection Area

Our sample is basically composed of three sections as shown in Fig.3-3(b). The first region is the detection area with uniform grating region, the second region is the propagation region with no grating and the third region is the input collection area with a chirped grating.

This step is combination of Flood exposure and IL (Interferometric Lithography) exposure to fabricate propagation region and detection region.

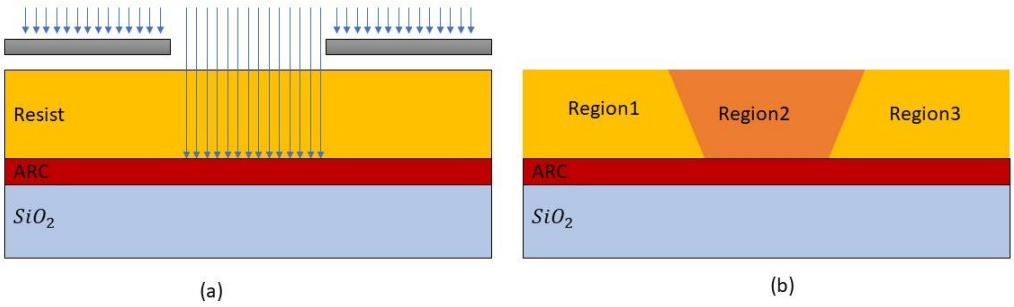

Figure 3-3: Flood exposure of the region 2 of the pixel to fabricate propagation region.

Step 1: The coated die with ARC and photoresist is exposed to UV exposure using a mask aligner in cleanroom. With exposure using a mask aligner, parallel light passes through the transparent areas of a photo mask onto the resist film (Fig.3-3(a)). The photo mask usually consists of a glass or quartz plate as carrier on which a thin lithographically patterned chromium coating forms the non-transparent pattern. For the existing mask aligner, the dimensions of the structures on the photo mask correspond to the dimensions of the exposed areas of the resist film, the image is thus congruent. When exposed to the UV light, the negative resist becomes crosslinked/polymerized, and more difficult to dissolve in developer.

Step 2: After flood exposure of the region two which is the propagation region, a uniform IL exposure is done in region one, which is detection region with a uniform grating. we have to shield region 3 from IL exposure at this step.

The Interferometric lithography set up used for uniform grating fabrication is shown schematically in Fig.3-4. Two coherent optical plane waves with the same polarization are symmetrically incident on a photosensitive layer coated onto a substrate at angles of $\pm\theta$.

The intensity pattern in space is simply given by

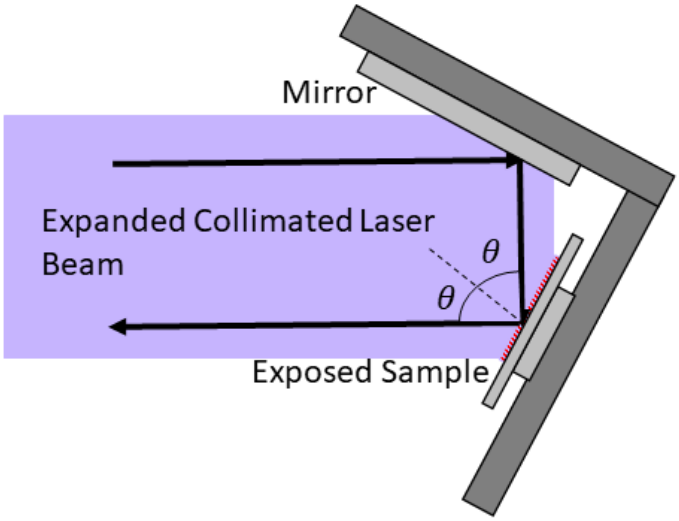

Figure 3-4: Experimental arrangement for IL.

$$\begin{aligned} I(x,z) &= |E|^2\left|\hat{e}_1 e^{ikx\sin\theta} + \hat{e}_2 e^{-ikx\sin\theta}\right|^2 \\ &= |E|^2\left[2 + \left(\hat{e}_1.\hat{e}_2{}^* e^{i2kx\sin\theta} + \hat{e}_1{}^*.\hat{e}_2 e^{-2ikx\sin\theta}\right)\right] \qquad (3-1) \\ &= 2|E|^2\left[1 + \sigma_{pol}\cos(2kx\sin\theta)\right] \end{aligned}$$

Where $k = \frac{2\pi n}{\lambda}$ with n the refractive index of the medium (one for air) and λ the optical wavelength and $\hat{e}_i$ is the unit polarization vector for each wave. The period of the interference pattern along the x direction is $\frac{\lambda}{2n\sin\theta}$ and for (TE, TM) polarization. $\sigma_{pol} = [1, \cos 2\theta]$ for (TE, TM) polarization.

TE polarization always gives the maximum contrast, while the contrast is reduced for TM polarization as a result of the π-phase shift between the $\hat{e}_x$ and $\hat{e}_z$ contributions to the interference intensity. As it is shown in Fig.3-4, the experimental setup is a simple corner cube arrangement (Fresnel mirror) where the right and left halves of the beam are folded onto each other using a $90°$ geometry. Thus when using interferometric lithography, the

photoresist is exposed with a sinusoidal irradiance pattern with a pitch defined by equation $\Lambda = \frac{\lambda}{2n \sin\theta}$.

The Laser used for the IL patterning in the fabrication of our collection area and detection area on chirped grating spectrometer is an Infinity 40-100 frequency tripled Nd:YAG laser from Coherent Inc. It is a Q-switched laser with output pulse duration of 3.0 ns, repetition rate adjustable in the range of 0.1 to 100 Hz. This laser has wavelength of 355 nm and maximum output power of about 16 W. Actual output power is controlled by setting the pulse energy and repetition rate. With a beam expander, laser raw beam is expanded to about 6 inches in diameter for large IL exposure area.

After exposure of the first and second region, we need to fabricate the collection area which is a chirped grating region.

Table 3-3: Recipe for uniform grating IL patterning.

Laser Infinity	Infinity 40-100
Laser Wavelength (nm)	355
UV Pulse Energy (mJ)	100
UV Pulse Energy Density (mJ/cm^2)	~3
Laser Pulse Repetition Rate (Hz	60
Exposure Time (Sec)	7.5

3.4 Chirped Grating Set up

Interference between two spherical wavefronts is utilized to fabricate a chirped grating. With that in mind, we designed this experimental setup for IL as shown in Fig 3-5. It is

basically a Lloyd mirror setup mounted on a rotation stage with an extra spherical lens mounted perpendicular to the mirror, which converts the collimated incident beam into the spherical waves for interference. Coordinate systems (X, Y, Z) and (X', Y') are drawn as shown in the schematic to help better explain how this setup works for our purpose. For the same reason, collimated coherent incident beam coming from the left-hand side is intentionally drawn in two separate circular cross-section portions. One portion of incident beam impinges on the spherical lens directly then gets converted to spherical wave by the lens and focused at point B. Likewise, the other portion of the incident beam, after being reflected by the mirror, shines onto the lens then gets converted and focused at point A. When a photoresist (PR) pre-coated sample is placed in the overlapped region of these two converging spherical waves as shown as the cone-shaped zone behind lens in the schematic, a quadratically chirped grating pattern will be registered in the PR layer.

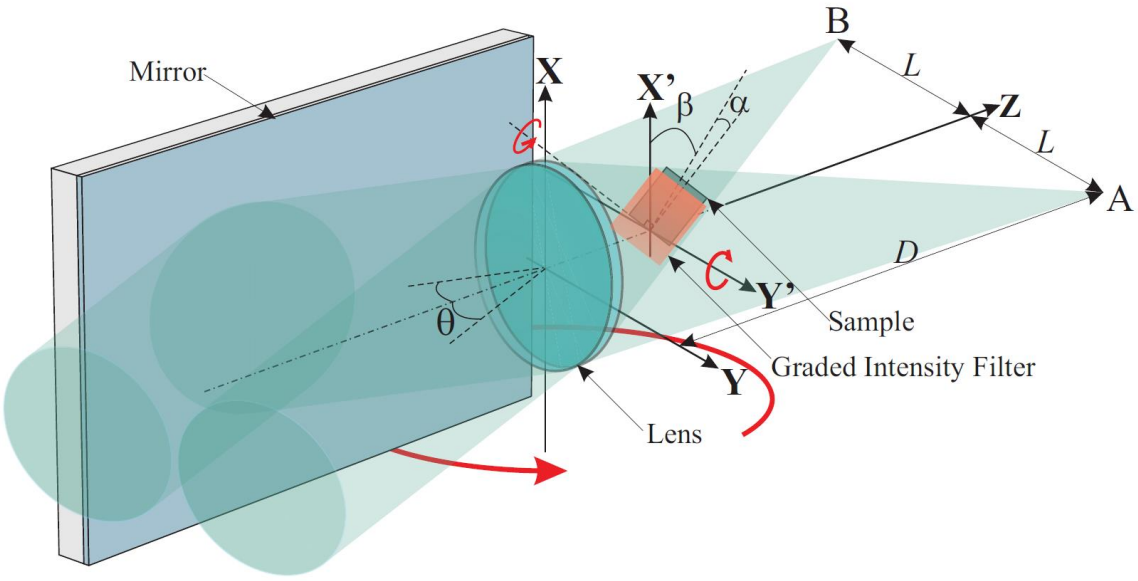

Figure 3-5: Interferometric lithography (IL) configuration with Lloyd mirror, lens, and sample placement.

As shown in the IL setup schematic of Fig. 3-5, incident beam falls into Y-Z plane and has incident angle of θ with respect to the axis Z or the optical axis of plano convex lens. Due to the particular geometric configuration of the optical elements in the IL experimental setup, foci A and B are also located in the Y-Z plane and are symmetric with respect to Z axis. In next section, the calculation of chirped grating period as function of location on the die surface is shown which is done in ref [37].

3.5 Calculation of Chirped Grating Period on Die

The derivation of the chirped grating period as function of location on the die surface

is to be done in such procedure explained below[37].

We define two coordinate systems, as shown in Fig.3-6: a three-dimensional space behind the lenses, with coordinates given as (x, y, z), with its origin at the back surface of the lenses on the symmetrical optical axis, and the coordinate system tied to the sample surface, whose coordinates are given as (u, v, w = 0), and whose origin lies on the symmetrical optical axis of the lenses, a distance *d* from the back face of the lens measured along the

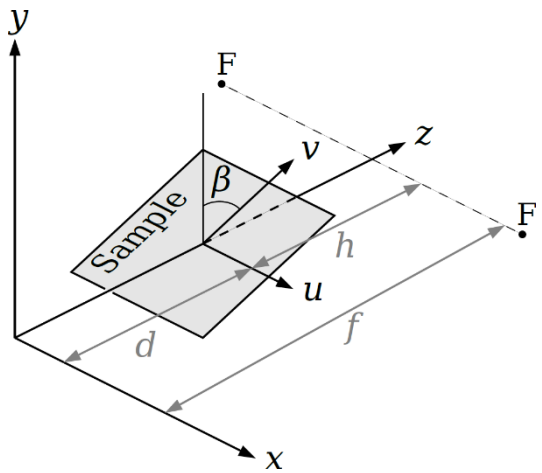

Figure 3-6: Coordinate systems, where z axis is optical axis of lens, the x – y plane is the back surface of lens, and foci lie in the x – y plane; (u, v) sample coordinates have origin on the z axis, u lies in the x – z plane, and v lies in the y – z plane, , at an angle of β to the y axis.

optical axis, and where the u axis lies in the x − z plane. A point (u, v, w = 0) in the sample plane has (x, y, z) spatial coordinates (u, v cos β, d + v sin β). The unit vectors in these systems are related by the simple rotational transform.

$$\left\{\hat{e}_x = \hat{e}_u;\ \hat{e}_y = \cos(\beta)\,\hat{e}_v - \sin(\beta)\,\hat{e}_w;\ \hat{e}_z = \sin(\beta)\,\hat{e}_v + \cos(\beta)\,\hat{e}_w\right\} \qquad (3\text{-}2)$$

Behind the lens, spherical waves converge toward the foci. The distances l_i from each of the two foci to a point (u,v,0) are given by:

$$l_i(u,v) = \sqrt{\left(u \pm f\sin\right)^2 + (v\cos\beta)^2 + (d + v\sin\beta - f\cos\theta)^2} \qquad (3\text{-}3)$$

$$i \in \{1,2\}$$

and the corresponding wavevectors are:

$$\vec{k}_i(u,v) = \frac{2\pi}{\lambda l_i(u,v)}\begin{bmatrix}\hat{e}_x(u \pm f\sin\theta) + \hat{e}_y(v\cos\beta)\\ +\hat{e}_z(d + v\sin\beta - f\cos\theta)\end{bmatrix}$$
$$= \frac{2\pi}{\lambda l_i(u,v)}\begin{bmatrix}\hat{e}_u(u \pm f\sin\theta) + \hat{e}_v(v + (d - f\cos\theta)\sin\beta)\\ +\hat{e}_w(d - f\cos\theta)\cos\beta\end{bmatrix} \qquad (3\text{-}4)$$

Then the grating period in the u direction is:

$$P_u(u,v) = \frac{\lambda}{\sin\theta_1 - \sin\theta_2} = \frac{\lambda}{\frac{u + L}{l_1(u,v)} - \frac{u - L}{l_2(u,v)}} \qquad (3\text{-}5)$$

in the v direction

$$P_v(u,v) = \lambda[v - (d - f\cos\theta)\sin\beta]\frac{1}{\left(\frac{1}{l_1(u,v)} - \frac{1}{l_2(u,v)}\right)} \qquad (3\text{-}6)$$

and the local pitch is given by

$$\frac{1}{P(u,v)} = \sqrt{\frac{1}{P_u^2(u,v)} + \frac{1}{P_v^2(u,v)}} \qquad (3\text{-}7)$$

Note that for $\beta = 0$, the sample normal to the optical axis, all of these expressions are even in u and v, and an approximately quadratic period dependence is expected in both directions. However for $\beta \neq 0$, P_u has a linear variation with v, while it remains quadratic in u. P_v remains even in both u and v.

In our fabrication set-up, $\beta = 45°$. Note that this tilt of the wafer is critical for obtaining a transversely chirped grating since it adds the impact of the focusing in the x direction on the wafer while leaving the y-direction unchanged with a small quadratic chirp.

3.6 Chirped Grating Patterning with IL

This step is actually combination of IL exposure, post exposure bake and development. In order to fabricate the chirped grating region on the region three, we need to use the IL set up for chirped grating which is shown in Fig.3-5. It is basically a Lloyd mirror setup mounted on a rotation stage with an extra spherical lens mounted perpendicular to the mirror, which converts the collimated incident beam into the spherical waves for interference.

When a photoresist (PR) pre-coated sample is placed in the overlapped region of the two converging spherical waves as shown as the cone-shaped zone behind lens in the schematic 3-5 a quadratically chirped grating pattern will be registered in the PR layer. After exposure the third region using this setup, a post-exposure bake (PEB) is performed before developing. Then, the sample is developed in developer MF-321 for 60 second.

The resultant structure is shown in Fig.3-7.

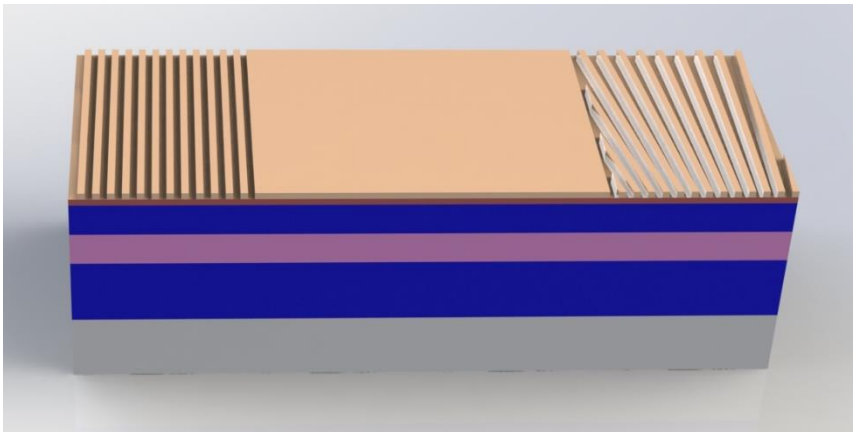

Figure 3-7: schematics of chirped grating spectrometer on photoresist.The chirped grating region is across 16mm width. For the present experiments, the propagation region is 1.2 cm long to allow for mounting of the commercial detector array.

Chirped IL Patterning Recipe is shown in table 3-4.

Table 3-4: Chirped Grating Fabrication Recipe.

Laser Infinity	Infinity 40-100
UV Pulse Energy (mJ)	100
UV Pulse Energy Density (mJ/cm^2)	~3
Laser Pulse Repetition Rate (Hz)	60
Exposure Time (Sec)	5.5
Post Exposure Bake (PEB) Temperature	110
Developer	MF-321
PEB Time (Sec)	60
Develop Time (Sec)	60

3.7 Grating Pattern Transfer

Both the chirped grating and the uniform grating patterned in the previous steps are transferred through ARC layer then ~350 nm into the top clad of the slab waveguide

structure on the die in a single etch step. Inductively coupled plasma etcher(ICP) from ADVANCED-VACCUM is used for this pattern transfer. Before real die is etched, dummy samples with same chirped grating are etched for different durations, and then measured under SEM for the grating depth to get the information of clad etch rate, etch profile and time to etch through ARC layer. Etch time of 350 nm deep grating on real device is then calculated based on the etch rate acquired through linear fitting of the etch data of the dummy samples. Recipe for grating pattern transfer with ICP is shown in table 3-5.

Table 3-5: Recipe for grating pattern transfer.

Etch Recipe	Step1: ARC etch recipe	Step2: SiO_2 etch recipe
Reactive Gas	O_2	CF_4
Reactive Gas Flow (sccm)	30	45
He Flow for Cooling (sccm))	10	10
Pressure (mTorr)	10	5
ICP Power (W)	350	400
RF Power (W)	25	100
DC Bias (V)	206	169
Temperature (◦C)	20	20
Etch Time (min)	1	2

3.8 Residual PR/ARC Removal

Once the grating pattern has been transferred into the die or top clad of the slab waveguide structure, residual PR and ARC are removed with reactive ion etcher (RIE), PlasmaLab RIE-80 from Oxford Instrument Inc. PR and ARC tend to be harder to remove after the grating pattern transfer process in ICP, so RIE etch time in the removal process is intentionally set to be long for a thorough removal with oxygen plasma, considering the

etch gas O_2 etches PR and ARC but not SiO_2 top clad. Recipe for residual PR and ARC removal is shown in table 3-6.

Table 3-6: Recipe for residual PR and ARC removal.

Etch Gas Mixture	O_2
Gas Flow(sccm)	15
Etch Pressure(mTorr)	10
RF Power (% of 300W)	15
DC Bias Reading(V)	190
Etch Time(min)	15

Fig.3-8 shows the final fabricated device. The chirped grating is across 16mm width and the length of the propagation region is 12 mm.

Figure 3-8: schematics of chirped grating spectrometer. The chirped grating region is across 16mm width. For the present experiments, the propagation region is 1.2 cm long to allow for mounting of the commercial detector array.

Chapter4

4.1 Device characterization

After fabrication of the chirped-grating spectrometer, we need to characterize the structure. For characterization of the device, first we measured the pitch in grating collection area and detection area. Then we measured the coupling length of the device. The tooth height and the initial top cladding thickness together control the coupling length. The coupling length, L_c, defines the collection area width for the incident light. After pitch and coupling length measurements, we measure the response of our spectrometer on chip to the laser source and LED light.

4.2 Pitch Measurements in Detection Area

The uniform grating region (detection area) on main sample had their pitch measured. The pitch measurements were all done optically by measuring the angle of diffraction from a laser beam projected on the grating samples.

The laser used was a green laser with $\lambda = 532\text{nm}$. The samples were mounted on a rotation stage perpendicular to the laser beam. A stepper motor with 1/40° resolution controls the rotation stage. A screen, with a small hole allowing the incoming laser beam through, is placed in the beam path in order to monitor the reflected/diffracted beam off the resist sample. Figure 4-1 shows the layout of the pitch measuring system.

As the laser beam is projected perpendicular to the sample, the resist pattern grating on the sample diffracts the incoming laser beam. The zero order of the diffracted beam is reflected directly back along the incoming laser beam (Figure 4-1a). The first orders are diffracted at an angle determined by the pitch on the wafer. The following formula gives the angle of the diffracted beam as a function of pitch.

$$\Lambda = \frac{\lambda}{2\sin\theta} \quad ,\theta = \text{Sin}^{-1}\frac{\lambda}{2\Lambda} \tag{4-1}$$

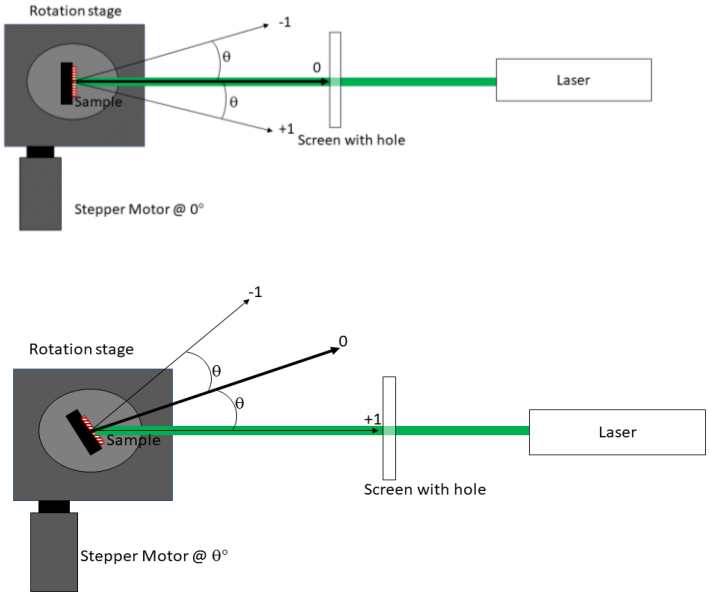

Figure 4-1: Layout of pitch measurement setup.

If the angle is known, then the pitch can be determined or vice versa. To determine the angle the rotation stage is turned until first diffracted order is reflected back along the incoming laser beam (Fig. 4-1b).

The accuracy of the angle is only determined by the resolution of the stepper motor and the ability to align the diffracted beam with the incoming beam.

Once the pitch of the grating is known, the width of the lines in the grating is estimated from the SEM image of the grating. Measuring the ratio of the linewidth to pitch of a grating from its SEM image and multiplying that ratio to the known pitch gives the estimated line width.

4.3 Pitch Measurements in Collection Area

The chirped grating spectrometer consists of a chirped collection area to receive the incident light and to couple a varying spectral portion into the waveguide as a function of the position across the coupling area.

The grating period in collection area as function of the position on the die is given by[56]:

$$\Lambda(x,y) = \frac{\lambda_{IL}}{\sqrt{\frac{(x+H)^2+y^2+D^2\sin^2\beta}{(x+H)^2+y^2+D^2} + \frac{x^2-H^2+y^2+D^2\sin^2\beta}{\sqrt{(x+H)^2+y^2+D^2}\sqrt{(x-H)^2+y^2+D^2}} + \frac{(x-H)^2+y^2+D^2\sin^2\beta}{(x-H)^2+y^2+D^2}}} \quad (4\text{-}2)$$

Where λ_{IL} is the 355 nm laser wavelength and (x, y) are the spatial coordinates on the die. $H = 27.13\,\text{mm}$, is the half separation between the two foci as function of the incident beam angles and $D = 79.5\,\text{mm}$, is the longitudinal distance from the two foci to the back

surface of the plano-convex lens. $\beta = 45°$, is the die tilt angle. After IL patterning of the photoresist, the pattern is transferred into the 450 nm thick SiO_2 top clad of the Si_3N_4 waveguide core using ICP to a depth of 350 nm.

In order to measure grating across chirped grating region, first we need to measure the effective index of the waveguide structure used in chirped grating spectrometer. For this measurement, we use a waveguide filter element with uniform grating regions for both collection area and detection area. The test waveguide filter element with uniform regions is as the same structure as the test chirped spectrometer except that the collection area is uniform and has the same pitch as the detection area grating region which in our case is 380 nm.

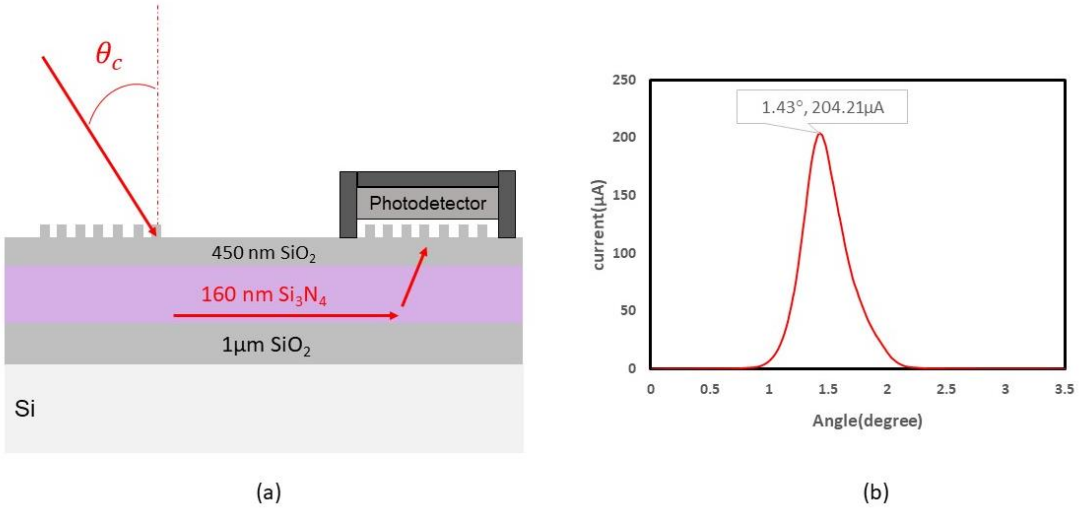

Figure 4-2: As we sweep the angle of illumination, The incident light is coupled to the waveguide at a specific wavelength and incident angle, providing a spectral/angular filtering function, and out-coupled from the waveguide downstream from the coupling region to a photodetector on top of the detection grating region.(b)Angular response of the waveguide filter element with uniform collection and detection area to the $\lambda = 660nm$.

To measure the effective index of the waveguide structure, first we need to register the angular response of the waveguide filter element with uniform grating regions.

As we sweep the angle of illumination, The incident light is coupled to the waveguide at a specific wavelength and incident angle, providing a spectral/angular filtering function, and

out-coupled from the waveguide downstream from the coupling region to a photodetector on top of the detection grating region as shown in Fig 4-2. From this angular response, we know the coupling angle. The wavelength and the grating pitch are also known (the grating pitch is 380 nm and the incident beam wavelength is 660 nm). Using equation below we could find the effective index of the waveguide structure in our chirped grating spectrometer.

$$\sin\theta_c \pm \frac{\lambda}{\Lambda(0,y)} = \pm n_{eff}^{TE,TM} \tag{4-3}$$

Where θ_c is coupling angle; λ is the wavelength of the incident light; Λ is the grating pitch and n_{eff} is the effective index of the waveguide.

The effective index of the waveguide for TE polarization is $n_{eff}^{TE} = 1.76$ and for TM polarization is $n_{eff}^{TM} = 1.65$ at $\lambda = 660$ nm.

From the FDTD simulation, the effective index of the waveguide for TE polarization is $n_{eff}^{TE} = 1.756$ and for TM polarization is $n_{eff}^{TM} = 1.642$ at $\lambda = 660$ nm.

As you can see, the simulation results and the measurement results are in a good agreement with each other.

Now, to measure the grating across the chirped grating area, we switch to the chirped spectrometer device. We need to record the angular response at each detector position.

The detector array that we used on top of the detection area to measure the angular response and to measure the pitch at chirped grating area is a Hamamatsu Si photodiode array(S4111-16R[58]) for UV to NIR. The S4111-16R is a Si photodiode linear array mounted in a ceramic DIP (Dual Inline Package). It has 16 pixels across our chirped grating

region. Each pixel is 0.9 mm wide. This photodiode array is primarily developed for low-light-level detection such as spectrophotometry and cover a wide spectral range from UV to near infrared light. Since all elements can be used with a reverse bias for charge storage readout, The S4111-16R is able to detect low level light with high sensitivity. Cross-talk between elements is minimized to maintain signal purity.

The features of the S4111-16R are:

- Large photosensitive area
- Low crosstalk
- Enhanced infrared sensitivity
- Low dark current

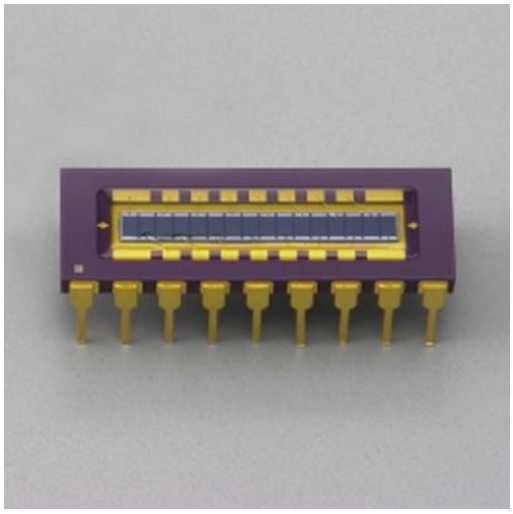

Figure 4-3: Hamamatsu S4111-16R Si Photodiode linear array.

Knowing the coupling angle of red laser at each detector position and the effective index of the waveguide, we can calculate the pitch at each detector using coupling equation 4-3.

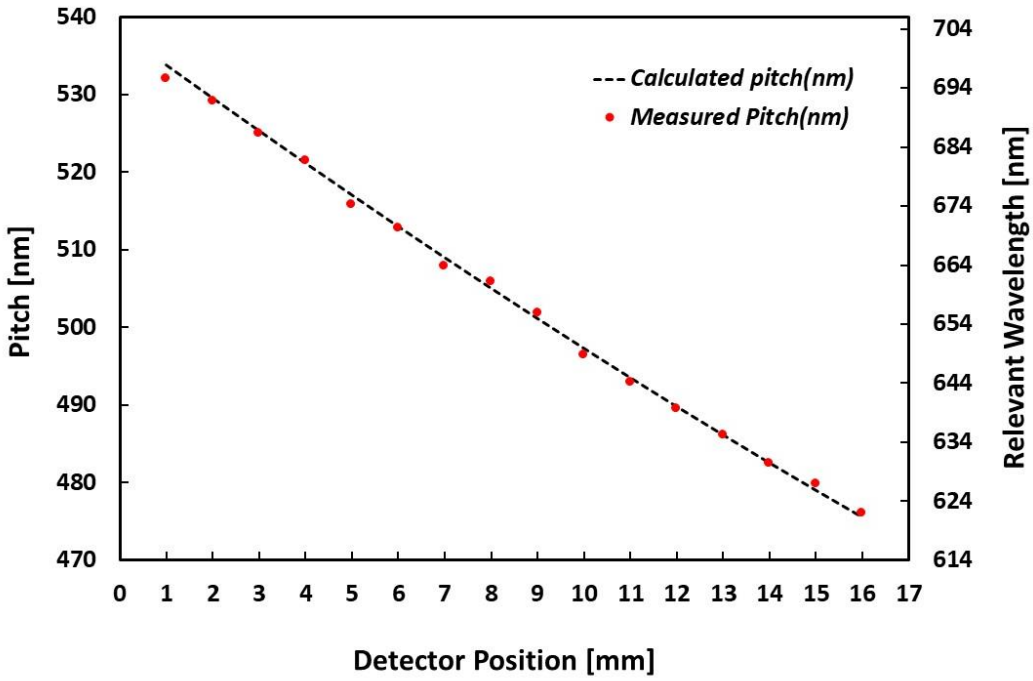

Figure 4-4: Measured grating period across the collection area compared with model calculation. The corresponding coupling wavelengths for TE polarization at an incident angle of $\theta_C = 27°$ are shown on the right axis.

Chirped grating period across a 16 mm wide collection area grating region is shown in Fig.4-4.

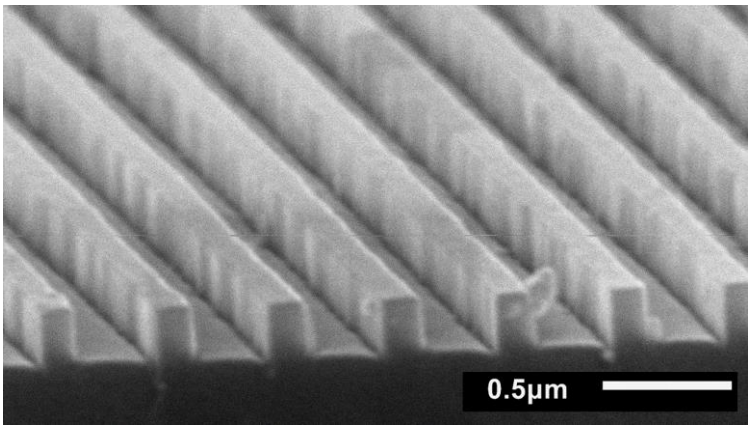

Figure 4-5: a SEM of a small region of the transversely chirped grating etched into the upper SiO_2 waveguide cladding (450 nm thick).

For the present device, the chirped grating covers a wavelength range of 70 nm over a width of 16 mm at a fixed angle of illumination $\theta_C = 27°$ and covers a pitch range of 50 nm over a width of 16mm. The fabricated chirp range defines spectral range. The calculated chirp grating period using equation 4-2, and the measured chirped grating period are in a good agreement. Fig.4-6 shows an image of fabricated chirped grating spectrometer with chirped grating area as collection area and uniform grating area as detection area. The grating regions are etched 350 nm into a 450 nm top cladding of the waveguide.

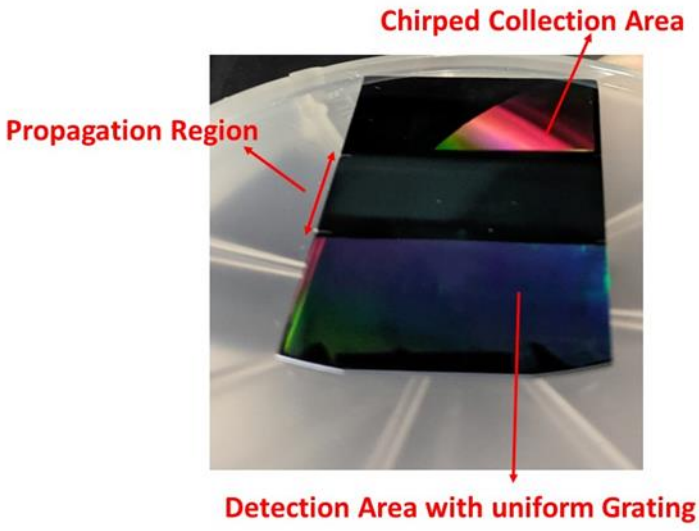

Figure 4-6: Image of the Fabricated chirped grating spectrometer.

4.4 Coupling Length Measurement

Coupling length, L_C, defines the collection area width for the incident light. The power coupled into the waveguide saturates at this distance due to the detailed balance between input coupling and re-radiation back into the free-space modes.

It is important to measure the coupling length because coupling length shows how much power is coupled into the waveguide structure. Also, for our structure, the resolution of the grating coupler is set by the smallest of the coupling length, L_C; the width of the source

illumination at the grating; or the physical width of the grating. In the current experiments, from simulation results we know that the L_C is ~ 305 μm. Since L_C is the smallest of the three parameters, the resolution of our structure is set by the coupling length.

Coupling length is found by source position sweep at resonant angle experiment. As the distance between center of ~ 1 mm diameter input laser beam (λ = 660nm) and the edge of the grating coupler increases, the transmitted power to the detection area decreases due to reradiation of the coupled power back into free space. The test grating coupler pitch is 380 nm and the grating is etched 360 nm into the 450 nm thick SiO_2 top cladding.

The power attenuation coefficient$\left(\alpha = \frac{1}{L_c}\right)$ or equivalently the grating coupling length is measured to be $L_c = 359$ μm for TE polarization using beam position sweep results. The results of experiment and model for the coupling length at λ = 660 nm is shown in Fig.4-7. The simulation results for coupling length, is $L_c = 305$ μm.

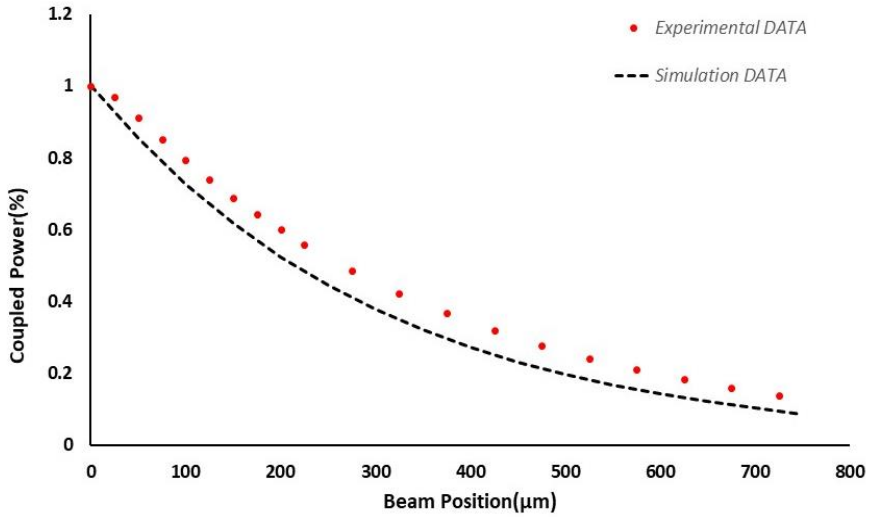

Figure 4-7: Experiment and modeling for TE coupling length evaluated by measuring the decay of the power transmitted to the detector region vs. position.

4.5 Device Operation and Results

Figure 4-8 shows the chirped-grating spectrometer concept. The input light is incident on a transversely chirped grating collection area; shielding is used to ensure that the detected light has coupled into the waveguide; the light propagates across the grating free region and is out-coupled at the detection region. Because of the local variation of the grating pitch across the collection area, different wavelengths of light are coupled into the waveguide at different lateral positions across the collection area. Guided light is then out-coupled with a second grating in the detection area and directed to an array of photodiodes placed either atop or below the second grating region. Spectral information is encoded in the chirped grating coupler, which is fabricated in a single lithography step, independent of the number of channels. For these initial experiments, a commercial, 1D CMOS detection array was used with a distance of ~ 2 mm between the grating out-coupler and the detector array.

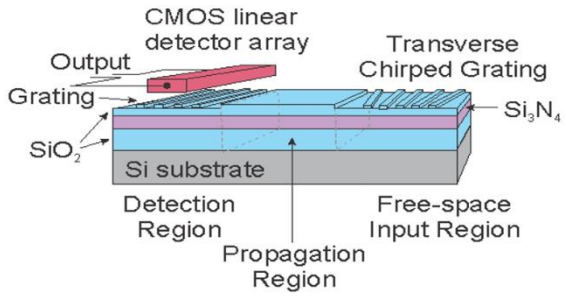

Figure 4-8: Schematic of the plenoptic spectrometer structure that consists of a transversely chirped grating collection region; a waveguide propagation region; and a detection region. For this proof-of-principle experiment the detector is a linear CMOS detector array on a separate chip. For the present experiments, the propagation region is 1.2 cm long to allow for mounting of the commercial detector array.

Figure 4-9 shows the spectrometer concept. The collimated input beam is incident at a fixed angle across the full width of the grating/detector combination. The spatially dependent grating period results in coupling only in a narrow spatial band for a narrow band source

as illustrated schematically. For the local chirp rate dd/dx ~3.3 nm/mm, the coupling resonance extends across a width of $\delta x = \delta d(dd/dx)^{-1} \sim 100$ μm (approximately 7 pixels for the present 14-μm wide detector pixels).

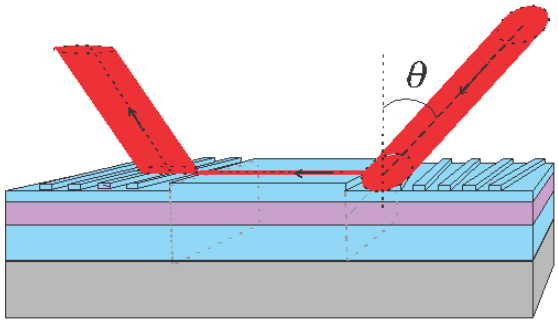

Figure 4-9:Conceptual diagram of the plenoptic spectrometer operation. Light is incident at an angle θ across the entire width of the chirped grating; the spatially varying grating pitch provides a filtering function that only couples the light into the waveguide where the grating equation is locally satisfied.

The coupled power propagates in the waveguide across the region with no grating and is coupled out by the second grating. For the present experiments, the propagation region is 1.2 cm long to allow for mounting of the commercial detector array. In an integrated version of the plenoptic spectrometer, this distance can be substantially decreased to ~ 100 μm or less, sufficient to provide good modal discrimination. The detector array (Hamamatsu S11639-01[59]; with 2048 14×200 μm^2 pixels) is mounted above the output grating and shielding is added to eliminate any light scattered directly to the detector. The detector array is 2.8 cm long. About 1150 pixels are within the 16 mm extent of the chirped grating. The detector array has 14 μm wide pixels providing sufficient sampling density for digitization given the resolution in δx of ~ 100 μm. Pixel values are read out sequentially with shift register electronics and an 8-bit A/D converter. A low-cost microcontroller (Raspberry Pi) is used to generate the timing signal and read the output of

the A/D for further processing.

Figure 4-10 shows the spectral measurement for a TE-polarized HeNe laser with an intrinsic linewidth much lower than the spectrometer resolution limits. The ~ 1 mm diameter output beam of the laser was directed to boundary between the chirped grating and the propagation region at an incident angle of ~ 31.8° to center the response relative to the detector array.

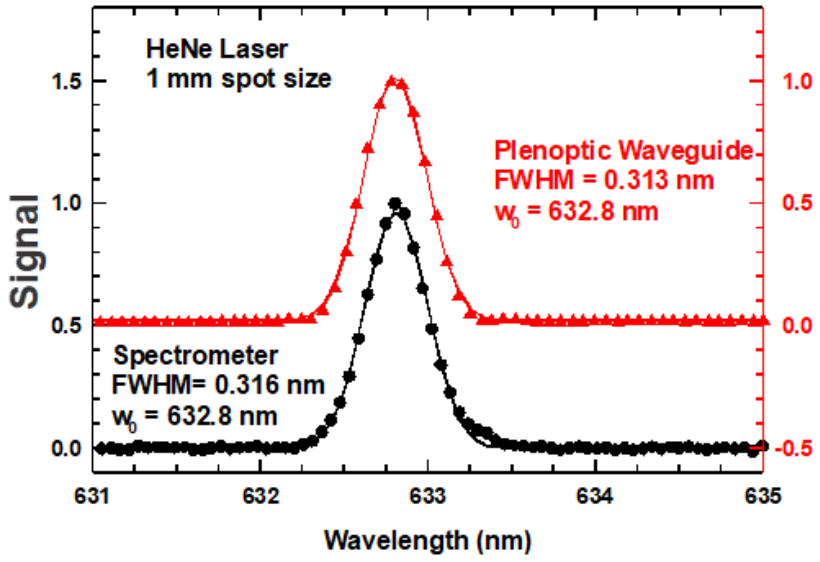

Figure 4-10:Spectral result for a HeNe laser beam with ~ 1 mm spot size. Results are compared for the plenoptic waveguide and a 1/4 m laboratory spectrometer. A resolution of 0.313 nm is achieved for the cur-rent grating chirp. The solid curves are least squares fits to Gaussian lineshapes.

A five-point moving average was used to reduce electronic readout noise with a 1 second integration time. The demonstrated resolution is 0.313 nm; the solid line is a least squares fit to a simple Gaussian lineshape in excellent agreement with the measurement. A conventional laboratory spectrometer system (1/4 m) provides essentially identical results. This resolution could be improved with weaker coupling, e.g. increased L_C.

From equation 2-16, $\delta\lambda \sim \frac{\lambda d}{2L_c(1-d\frac{\partial n}{\partial \lambda})}$, at a wavelength of 632.8 nm for an L_C of ~ 360 µm,

the calculated resolution is $\delta\lambda \sim 0.37$ nm. The waveguide dispersion ($\frac{\partial n}{\partial \lambda} \sim 0.00041\ \mathrm{nm}^{-1}$) includes both material and structural components.

As you can see the measurement result, $\delta\lambda \sim 0.313$ nm and the calculation result, $\delta\lambda \sim 0.37$ nm is in a good agreement.

The result for a red LED along with a polarizer set to transmit TE polarization is shown in Fig.4-11 along with a comparison with a laboratory scale spectrometer. The peak wavelength for LED is $\lambda = 623.5$ nm. The angle of incidence of the LED beam is tuned to 31.8°, to shift the response to the center of the detector. The blue tail of the LED is clearly observed. Note the very different wavelength scale as compared with the laser result. Again, a five-point moving average was used with a 1sec s integration time.

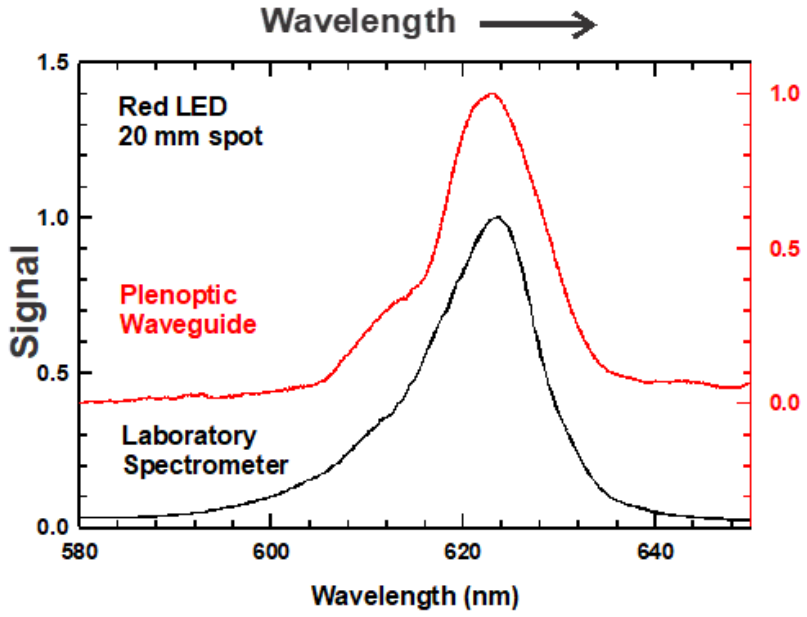

Figure 4-11:Spectral result for a red LED incident across the entire width of the chirped grating with equivalent results from a laboratory spectrometer and the plenoptic array.

In our structure, the TE and TM polarizations exhibit different effective indices and, therefore, different coupling angles. This is shown in Fig. 4-12 where a red diode laser at 660 nm was used as a source. The beam was spread to cover the full range of the chirped grating and was incident at 22° with the polarization set at ~ 45° to the grating lines. As expected, two peaks are observed corresponding to TE and TM polarizations.

This dual response at the same wavelength can be eliminated with the use of an external polarizer. Alternatively, since the TM mode is more loosely bound (lower effective refractive index) it is possible to engineer the bottom oxide thickness to selectively absorb the TM mode while having no impact on the TE mode intensity.

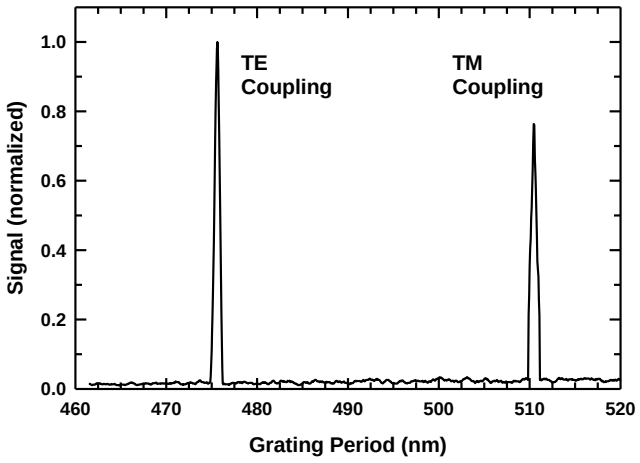

Figure 4-12:Because the effective indices differ for TE and TM polarization, the coupling angles are different for the two polarizations. Result for a 660 nm red laser incident at 22° from the normal.

Chapter5

5.1 Conclusion and Outlook

A plenoptic spectrometer comprising a transversely chirped grating waveguide coupler along with a propagation region to eliminate non-propagating (cut-off) modes and a second grating for out-coupling has been demonstrated as a fully CMOS-compatible plenoptic spectrometer. For the present preliminary demonstration, an externally mounted, 2048 element linear array CMOS detector was used to capture the spectrum. For a HeNe laser, a linewidth FWHM of 0.313 nm has been demonstrated. This resolution is a direct result of the chirped grating physics and does not need any signal processing deconvolution. The fabrication process involves only a single lithography step that is well within the capabilities of IC industry lithography tools.

There are many directions for further optimization of these results. The use of chirped grating within desired ranges over a sample of particular size, will allow adjustment of the spectral/angular width to adjust the spectral width to match visible spectrum of 400- to 700-nm and to assure complete spectral coverage within a fixed angle of illumination. In order to fabricate a collection area with a chirped range enough to couple the whole visible

spectrum at a fixed angle of illumination, there is a need to build a new Chirped IL set-up using two cylindrical lenses. In order to measure the spectrum of the light across the entire visible (400-700 nm) at a fixed angle of illumination, the chirped collection area should have 205 nm chirp range. To design a chirped grating coupler with chirp range of 205 nm, we need a new interferometric lithography with cylindrical lens configuration in which two cylindrical lenses oriented in a way that angle between their focal lines is $\alpha = 45°$ and the incident angle is $\theta = 24.77°$. For this specific application, cylindrical lens should be identical with focal length of $f = 16.2$ cm ($R_1 = R_2 = 7.7$ cm, $t = 7$ mm). This setting and configuration is able to fabricate a chirped grating coupler with chirp range of 220 nm across 10 mm width[37].

So far, in order to characterize our chirped grating spectrometer, we used a commercial detector array. Since our device is fully CMOS compatible, in future the detector region can be fabricated on the underlying silicon wafer and achieve a fully integrated device.

As was discussed above, the TE and TM polarizations exhibit different effective indices and, therefore, different coupling angles. This splitting can be eliminated with the use of an external polarizer. Alternatively, since the TM mode is more loosely bound (lower effective refractive index) it is possible to engineer the bottom oxide thickness to selectively absorb the TM mode while having minimal impact on the TE mode intensity.

There are many applications for inexpensive, compact, low profile, robust, vibration-insensitive, integrated, solid-state visible spectrometers ranging from chemical and environmental monitoring to industrial process control. The chirped grating spectrometer we have described will find application across many of these areas. The spectral resolution can be structurally tuned across a wide range from less than 1 nm to more than 100 nm

providing a wide range of functionality. The use of integrated avalanche photodetectors can extend the sensitivities to photon counting applications. The same concept can be extended to other wavelength ranges with different detector material systems, extending the range of applications.

Appendix A

Lists of the Lumerical codes used in this dissertation.

Listing1.

 # wg_2D_draw.lsf - draw the waveguide geometry in Lumerical MODE

```
newmode; newmode; redrawoff;

# define wafer and waveguide structure

thick_Clad = 0.1e-6;

thick_wg   = 0.16e-6;

thick_BOX  = 1e-6;

thick_Wafer =2e-6;

# define materials

#material_Clad = "SiO2(CHA)";

material_Clad  = "SiO2(LPCVD)";

material_BOX = "SiO2(LPCVD)";

material_wg = "Si3N4(LPCVD)";

material_Wafer = "Si (Silicon) - Palik";

#define simulation region

width_margin = 1e-6;  # space to include on the side of the waveguide

height_margin =2.5e-6; # space to include above and below the waveguide

# calculate simulation volume

# propagation in the x-axis direction; z-axis is wafer-normal

Xmin = -2e-6; Xmax = 2e-6; # length of the waveguide
```

```
Zmin = -height_margin;Zmax = height_margin+thick_wg;
Y_span = 2*width_margin; Ymin = -Y_span/ 2; Ymax = -Ymin;
# draw silicon wafer
addrect;
set("name", "Wafer");
set("material", material_Wafer);
set("x min", Xmin); set("x max",Xmax);
set("z max", -thick_BOX); set("z min", -thick_Wafer - thick_BOX);
set("y", 0); set("y span", Y_span+1e-6);
# draw buried oxide
addrect;
set("name", "BOX");
set("material", material_BOX);
set("x min", Xmin); set("x max", Xmax);
set("z min", -thick_BOX); set("z max",0);
set("y", 0); set("y span", Y_span +1e-6);
#draw waveguide
addrect; set("name", "waveguide");
set("material", material_wg);
set("y", 0); set("y span", Y_span +1e-6);
set("z min",0); set("z max",thick_wg);
set("x min", Xmin); set("x max", Xmax);
# draw cladding
```

```
addrect;
set("name","Clad");
set("material", material_Clad);
set("y", 0); set("y span", Y_span + 1e-6);
set("z min",thick_wg); set("z max",thick_wg + thick_Clad);
set("x min", Xmin); set("x max", Xmax);
```

Listing2

```
# wg_1D_slab.lsf - setup the Lumerical MODE 1D simulation
wg_2D_draw; # draw the waveguide
wavelength = 0.660e-6;
meshsize = 10e-9; # mesh size
# add 1D mode solver (waveguide cross-section)
addfde;
set("solver type","1D Z:X prop");
set("x", 0); set("y", 0);
set("z max",Zmax ); set("z min", Zmin);
set("wavelength", wavelength);
set("define z mesh by","maximum mesh step");
set("dz", meshsize);
modes = 4; # modes to output
set("number of trial modes", modes);
```

Listing3

 # wg_1D_slab_mode.lsf - calculate mode profiles in Lumerical MODE

```
 wg_1D_slab; # Draw waveguides and setup the simulation
n = findmodes; # calculate the modes
 for (m = 1: modes) {
?neff =real(getdata("FDE::data::mode"+num2str(m),"neff"));
z =getdata("FDE::data::mode1","z");
E3 = pinch(getelectric("FDE::data::mode"+num2str( m)));
plot( z, E3);   # plot the mode profile
}
```

Listing4: Plenoptic pixel 2D FDTD simulation – parameters;

initial_parameters.lsf

```
clear;
# define simulation parameters
wl_span=0.5e-6; # wavelength span
mesh_accuracy=3;
frequency_points=100;
simulation_time=1000e-15; # maximum simulation time [s]

# define grating coupler properties
pitch=0.38e-6; # gratingpitch
DC=0.5; # duty cycle
gc_number=100; # number of gratings
etch_depth=0.350e-6;# etch depth;
input_length=10e-6;
output_length=10e-6;

# define waveguide structure
```

```
thick_wg=0.16e-6; # thickness of nitride waveguide
thick_BOX=1e-6; # thickness of the bottom cladding
thick_Clad=0.45e-6; # thickness of the top cladding material
Si_substrate=4e-6; # thickness of the silicon substrate materials;
width_wg=0.5e-6; # width of the waveguide
# define materials
material_Clad = "SiO2(CHA)";
material_Clad = "SiO2(LPCVD)";
material_BOX = "SiO2(LPCVD)";
material_wg = "Si3N4(LPCVD)";
material_Wafer = "Si (Silicon) - Palik";

# define Gaussian source parameters
theta0=20; # incident angle
polarization='TE'; # TE or TM
lambda=0.66e-6; # wavelength
Position=30e-6; # position of the optical source on GC
```

Listing5: Plenoptic pixel 2D FDTD simulation – Plenoptic;

```
redrawoff;
gap=pitch*(1-DC); # etched region of the grating
# add Input Grating Coupler base
addrect; set('name','In_GC_base');
set('material',material_Clad);
set('x max',(gc_number+1)*pitch);
set('x min',0);
set('y',0.5*(%thick_Clad%-%etch_depth%));
set('y span',%thick_Clad%-%etch_depth%);
# add GC teeth;
for(i=0:gc_number)
{ addrect; set('name','GC_tooth');
set('material',material_Clad);
```

```
set('y',0.5*thick_Clad);
set('y span',thick_Clad);
set('x min',gap+i*pitch);
set('x max',pitch+i*pitch); }
selectpartial('GC');
addtogroup('In_gC');
# add output waveguide
addrect; set('name','In_GC_base');
set('material',material_Clad);
set('x min',(gc_number+1)*pitch);
set('x max',(gc_number+1)*pitch+%input_length%);
set('y',0.5*(%thick_Clad%-%etch_depth%));
set('y span',%thick_Clad%-%etch_depth%);
# add output Grating Coupler base
addrect; set('name','out_GC_base');
set('material',material_Clad);
set('x max',2*(gc_number+1)*pitch+%input_length%);
set('x min',(gc_number+1)*pitch+%input_length%);
set('y',0.5*(%thick_Clad%-%etch_depth%));
set('y span',%thick_Clad%-%etch_depth%);
# add GC teeth;
for(i=0:gc_number)
{ addrect; set('name','GC_tooth');
set('material',material_Clad);
set('y',0.5*thick_Clad);
set('y span',thick_Clad);
set('x min',(gc_number+1)*pitch+%input_length%+gap+i*pitch);
set('x max',(gc_number+1)*pitch+%input_length%+pitch+i*pitch); }
selectpartial('GC');
addtogroup('out_gC');
```

```
#draw waveguide

addrect; set("name", "waveguide");
set("material", material_wg);
set("x min",0); set("x max",2*(gc_number+1)*pitch+%input_length%);
set("y max",0);
set("y min",-thick_wg);

#draw silicon substrate

addrect; set("name", "wafer");
set("material", material_Wafer);
set("x min",0); set("x max",2*(gc_number+1)*pitch+%input_length%);
set("y max",-thick_wg-thick_BOX);
set("y min",-thick_wg-thick_BOX-Si_substrate);

#draw bottom cladding

addrect; set("name", "BOX");
set("material", material_BOX);
set("x min",0); set("x max",2*(gc_number+1)*pitch+%input_length%);
set("y max",-thick_wg);
set("y min",-thick_wg-thick_BOX);
```

Listing6: Plenoptic pixel 2D FDTD simulation – simulation setup for Gaussian beam;

Source_Gaussian.lsf

```
# 2D Plenoptic pixel Model with Gaussian input
deleteall;
initial_parameters;
```

```
Plenoptic;
# add simulation region;
addfdtd;
set('dimension','2D');
set('x min',2*pitch);
set('x max',2*(gc_number+1)*pitch+%input_length%-2*pitch);
set('y min',-(thick_BOX+0.2e-6));
set('y max',thick_Clad+2e-6);
set('mesh accuracy',mesh_accuracy);
set('simulation time',simulation_time);
# add input monitor;
addpower;
set('name','input');
set('monitor type','2D X-normal');
set('x',(gc_number+1)*pitch);
set('y',-0.5*thick_BOX);
set('y span',1.2e-6);

# add output monitor;
addpower;
set('name','output');
set('monitor type','2D X-normal');
set('x',(gc_number+1)*pitch+%input_length%);
set('y',-0.5*thick_BOX);
set('y span',1.2e-6);
# add T1 monitor;
addpower;
set('name','T1');
set('monitor type','2D X-normal');
set('x',1.5*(gc_number+1)*pitch+%input_length%);
set('y',-0.5*thick_BOX);
```

```
set('y span',1.2e-6);
# add Tup monitor;
addpower;
set('name','Tup');
set("monitor type",6);
set('x min',(gc_number+1)*pitch+%input_length%);
set('x max',2*(gc_number+1)*pitch+%input_length%);
set('y',thick_Clad+0.5e-6);
# add Tdown monitor;
addpower;
set('name','Tdown');
set("monitor type",6);
set('x min',(gc_number+1)*pitch+%input_length%);
set('x max',2*(gc_number+1)*pitch+%input_length%);
set('y',-thick_BOX+0.5e-6);
# add Gaussian mode
addgaussian;
set('name','source');
set('injection axis','y');
set('x',Position);
set('x span', 3*(gc_number+1)*pitch+%input_length%);
set('direction','Backward');
set('y',thick_Clad+1e-6);
if(polarization=='TE')
{ set('polarization angle',90); }
else{ set('polarization angle',0); }
set('angle theta',theta0);
set('center wavelength',lambda);
set('wavelength span',wl_span);
set('waist radius w0',5-6);
set('distance from waist',20e-6);
```

```
# global properties setglobalmonitor(’frequency points’,frequency_points);
setglobalmonitor('use linear wavelength spacing',1);
setglobalmonitor('use source limits',1);
setglobalsource('center wavelength',lambda);
```

Listing7: Plenoptic pixel 2D FDTD simulation – parameter sweeps; Plenoptic_sweeps.lsf

```
# Sweep various parameters of the grating coupler
newproject;
# Choose one of the following:
Sweep_type = 'pitch'# Period of the grating
#Sweep_type = ’FillFactor’;
# Fill factor of the grating
#Sweep_type = ’Position’; # Position of the optical source on the grating
#Sweep_type = ’Angle’;# Angle of the gaussian beam
#Sweep_type = ’BOX’;# Thickness of the buried oxide
#Sweep_type = ’Cladding’; # Thickness of the cladding
#Sweep_type = ’EtchDepth’; # Etch depth on the silicon grating GC_init;
if (Sweep_type == 'pitch') {
sweep_start = 0.3e-6;
sweep_end = 0.4e-6;
loop = 5; }
if (Sweep_type == 'Duty Cycle')
{ sweep_start = 0.4; sweep_end = 0.6; loop = 5; }
if (Sweep_type == 'Position') { sweep_start = 20e-6; sweep_end = 30e-6; loop =
10; }
if (Sweep_type == 'Angle') { sweep_start = 0; sweep_end = 30; loop = 5; }
if (Sweep_type == 'BOX') { sweep_start = 1e-6; sweep_end = 4e-6; loop = 50; }
if (Sweep_type == 'Cladding') { sweep_start = 0.1e-6; sweep_end = 0.5e-6; loop
= 50; }
```

```
if (Sweep_type == 'EtchDepth') { sweep_start = 0.06e-6; sweep_end = 0.3e-6;
loop = 5; }

M_sweep = linspace(sweep_start, sweep_end, loop);
M_Tlambda = matrix(loop,1); # matrix to store transmission at central wavelength
M_T = matrix(frequency_points,loop); # matrix to store transmission for all
wavelengths
for(ii=1:loop) { ? ii;
if (Sweep_type == 'pitch') { period = M_sweep(ii,1); }
if (Sweep_type == 'Duty Cycle') {ff = M_sweep(ii,1); }
if (Sweep_type == 'Position') { Position = M_sweep(ii,1); }
if (Sweep_type == 'Angle') { theta0 = M_sweep(ii,1); }
if (Sweep_type == 'BOX') { thick_BOX = M_sweep(ii,1); }
if (Sweep_type == 'Cladding') { thick_Clad = M_sweep(ii,1); }
if (Sweep_type == 'EtchDepth') { etch_depth = M_sweep(ii,1); }
switchtolayout;
selectall;
delete;
redrawoff;
Source_Gaussian;
run; T = transmission('input');
M_T(1:frequency_points,ii) = T;
M_Tlambda(ii,1) = T(floor(frequency_points/2));
switchtolayout; }
WL=linspace(lambda-0.5*wl_span,lambda+0.5*wl_span,frequency_points);
for(jj=1:loop) { plot(WL, abs(M_T(1:frequency_points,jj))); holdon; }
?10*log10(max(abs(M_T))); # lowest insertion loss
holdoff;
plot(M_sweep, abs(M_Tlambda));
```

References

[1] C. P. Bacon, Y. Mattley, and R. DeFrece, "Miniature spectroscopic instrumentation: Applications to biology and chemistry," *Review of Scientific Instruments*, vol. 75, no. 1, pp. 1–16, Dec. 2003.

[2] R. F. Wolffenbuttel, "State-of-the-art in integrated optical microspectrometers," *IEEE Transactions on Instrumentation and Measurement*, vol. 53, no. 1, pp. 197–202, Feb. 2004.

[3] T. Rasmussen, "Transmission grating based spectrometers," p. 9, 2010.

[4] "How Does a Spectrometer Work?" [Online]. Available: http://bwtek.com/spectrometer-introduction/. [Accessed: 27-Jun-2019].

[5] M. Vaughan, *The Fabry-Perot Interferometer : History, Theory, Practice and Applications*. Routledge, 2017.

[6] "Fabry–Perot cavity pulsed Fourier transform microwave spectrometer with a pulsed nozzle particle source: Review of Scientific Instruments: Vol 52, No 1." [Online]. Available: https://aip.scitation.org/doi/abs/10.1063/1.1136443. [Accessed: 14-Jul-2019].

[7] P. W. Atkins, J. De Paula, and J. Keeler, "Atkins' Physical chemistry /," *Olin College Library Catalog*. [Online]. Available: https://olin.tind.io/record/1640052. [Accessed: 27-Jun-2019].

[8] M. Florjańczyk, P. Cheben, S. Janz, A. Scott, B. Solheim, and D.-X. Xu, "Multiaperture planar waveguide spectrometer formed by arrayed Mach-Zehnder interferometers," *Opt. Express, OE*, vol. 15, no. 26, pp. 18176–18189, Dec. 2007.

[9] H. Podmore *et al.*, "Demonstration of a compressive-sensing Fourier-transform on-chip spectrometer," *Opt. Lett., OL*, vol. 42, no. 7, pp. 1440–1443, Apr. 2017.

[10] B. I. Akca, "Design of a compact and ultrahigh-resolution Fourier-transform spectrometer," *Opt. Express, OE*, vol. 25, no. 2, pp. 1487–1494, Jan. 2017.

[11] "Spatial heterodyne spectroscopy for high speed measurements of Stark split neutral beam emission in a high temperature plasma: Review of Scientific Instruments: Vol 89, No 10." [Online]. Available: https://aip.scitation.org/doi/abs/10.1063/1.5039285. [Accessed: 27-Jun-2019].

[12] A. Sharkawy, S. Shi, and D. W. Prather, "Multichannel wavelength division multiplexing with photonic crystals," *Appl. Opt., AO*, vol. 40, no. 14, pp. 2247–2252, May 2001.

[13] Z. Xia *et al.*, "High resolution on-chip spectroscopy based on miniaturized microdonut resonators," *Opt. Express, OE*, vol. 19, no. 13, pp. 12356–12364, Jun. 2011.

[14] B. B. C. Kyotoku, L. Chen, and M. Lipson, "Sub-nm resolution cavity enhanced micro-spectrometer," *Opt. Express, OE*, vol. 18, no. 1, pp. 102–107, Jan. 2010.

[15] B. E. Little *et al.*, "Ultra-compact Si-SiO2microring resonator optical channel dropping filters," *IEEE Photonics Technology Letters*, vol. 10, no. 4, pp. 549–551, Apr. 1998.

[16] A. Nitkowski, L. Chen, and M. Lipson, "Cavity-enhanced on-chip absorption spectroscopy using microring resonators," *Opt. Express, OE*, vol. 16, no. 16, pp. 11930–11936, Aug. 2008.

[17] Z. Wang *et al.*, "Single-shot on-chip spectral sensors based on photonic crystal slabs," *Nature Communications*, vol. 10, no. 1, p. 1020, Mar. 2019.

[18] S. Xie, Y. Meng, J. Bland-Hawthorn, S. Veilleux, and M. Dagenais, "Silicon Nitride/Silicon Dioxide Echelle Grating Spectrometer for Operation Near 1.55 µm," *IEEE Photonics Journal*, vol. 10, no. 6, pp. 1–7, Dec. 2018.

[19] F. Horst, W. M. J. Green, B. J. Offrein, and Y. A. Vlasov, "Silicon-on-Insulator Echelle Grating WDM Demultiplexers With Two Stigmatic Points," *IEEE Photonics Technology Letters*, vol. 21, no. 23, pp. 1743–1745, Dec. 2009.

[20] P. Cheben *et al.*, “A high-resolution silicon-on-insulator arrayed waveguide grating microspectrometer with sub-micrometer aperture waveguides,” *Opt. Express, OE*, vol. 15, no. 5, pp. 2299–2306, Mar. 2007.
[21] G. Micó, B. Gargallo, D. Pastor, and P. Muñoz, “Integrated Optic Sensing Spectrometer: Concept and Design,” *Sensors*, vol. 19, no. 5, p. 1018, 2019.
[22] M. K. Smit and C. V. Dam, “PHASAR-based WDM-devices: Principles, design and applications,” *IEEE Journal of Selected Topics in Quantum Electronics*, vol. 2, no. 2, pp. 236–250, Jun. 1996.
[23] Z. J. Sun, K. A. McGreer, and J. N. Broughton, “Demultiplexer with 120 channels and 0.29-nm channel spacing,” *IEEE Photonics Technology Letters*, vol. 10, no. 1, pp. 90–92, Jan. 1998.
[24] B. Momeni *et al.*, “Compact wavelength demultiplexing using focusing negative index photonic crystal superprisms,” *Opt. Express, OE*, vol. 14, no. 6, pp. 2413–2422, Mar. 2006.
[25] A. Emadi, H. Wu, G. de Graaf, and R. Wolffenbuttel, “Design and implementation of a sub-nm resolution microspectrometer based on a Linear-Variable Optical Filter,” *Opt. Express, OE*, vol. 20, no. 1, pp. 489–507, Jan. 2012.
[26] B. Redding, S. F. Liew, R. Sarma, and H. Cao, “Compact spectrometer based on a disordered photonic chip,” *Nature Photonics*, vol. 7, no. 9, pp. 746–751, Sep. 2013.
[27] S. A. Khan and A. K. E. Bowden, “Colloidal Quantum Dots for Cost-effective, Miniaturized, and Simple Spectrometers,” *Clinical Chemistry*, vol. 62, no. 4, pp. 548–550, Apr. 2016.
[28] J. Bao and M. G. Bawendi, “A colloidal quantum dot spectrometer,” *Nature*, vol. 523, no. 7558, pp. 67–70, Jul. 2015.
[29] K. M. Bryan, Z. Jia, N. K. Pervez, M. P. Cox, M. J. Gazes, and I. Kymissis, “Inexpensive photonic crystal spectrometer for colorimetric sensing applications,” *Opt. Express, OE*, vol. 21, no. 4, pp. 4411–4423, Feb. 2013.
[30] S.-W. Wang *et al.*, “Concept of a high-resolution miniature spectrometer using an integrated filter array,” *Opt. Lett., OL*, vol. 32, no. 6, pp. 632–634, Mar. 2007.
[31] Y. Tsur and A. Arie, “On-chip plasmonic spectrometer,” *Opt. Lett., OL*, vol. 41, no. 15, pp. 3523–3526, Aug. 2016.
[32] Y. Horie, A. Arbabi, E. Arbabi, S. M. Kamali, and A. Faraon, “Wide bandwidth and high resolution planar filter array based on DBR-metasurface-DBR structures,” *Opt. Express, OE*, vol. 24, no. 11, pp. 11677–11682, May 2016.
[33] M. Faraji-Dana, E. Arbabi, A. Arbabi, S. M. Kamali, H. Kwon, and A. Faraon, “Compact folded metasurface spectrometer,” *Nat Commun*, vol. 9, no. 1, pp. 1–8, Oct. 2018.
[34] N. K. Pervez, W. Cheng, Z. Jia, M. P. Cox, H. M. Edrees, and I. Kymissis, “Photonic crystal spectrometer,” *Opt. Express, OE*, vol. 18, no. 8, pp. 8277–8285, Apr. 2010.
[35] C. Peroz *et al.*, “Digital spectrometer-on-chip fabricated by step and repeat nanoimprint lithography on pre-spin coated films,” *Microelectronic Engineering*, vol. 88, no. 8, pp. 2092–2095, Aug. 2011.
[36] A. Neumann, J. Ghasemi, S. Nezhadbadeh, X. Nie, P. Zarkesh-Ha, and S. R. J. Brueck, “CMOS-compatible plenoptic detector for LED lighting applications,” *Opt. Express, OE*, vol. 23, no. 18, pp. 23208–23216, Sep. 2015.
[37] S. Benoit and S. R. J. Brueck, “Design of Chirped Gratings Using Interferometric Lithography,” *IEEE Photonics Journal*, vol. 10, no. 2, pp. 1–13, Apr. 2018.
[38] S. S. Wang and R. Magnusson, “Theory and applications of guided-mode resonance filters,” *Appl. Opt., AO*, vol. 32, no. 14, pp. 2606–2613, May 1993.
[39] Z. Zhu and T. G. Brown, “Full-vectorial finite-difference analysis of microstructured optical fibers,” *Opt. Express, OE*, vol. 10, no. 17, pp. 853–864, Aug. 2002.

[40] "Optical Waveguide Design Software - Lumerical MODE," *Lumerical*. [Online]. Available: https://www.lumerical.com/products/mode/. [Accessed: 15-Jul-2019].
[41] L. Chrostowski and M. Hochberg, *Silicon Photonics Design: From Devices to Systems*. Cambridge University Press, 2015.
[42] "Nanophotonic FDTD Simulation Software - Lumerical FDTD," *Lumerical*. [Online]. Available: https://www.lumerical.com/products/fdtd/. [Accessed: 15-Jul-2019].
[43] D. Sullivan, Jun Liu, and M. Kuzyk, "Three-dimensional optical pulse simulation using the FDTD method," *IEEE Transactions on Microwave Theory and Techniques*, vol. 48, no. 7, pp. 1127–1133, Jul. 2000.
[44] K. Ogawa, W. Chang, B. Sopori, and F. Rosenbaum, "A theoretical analysis of etched grating couplers for integrated optics," *IEEE Journal of Quantum Electronics*, vol. 9, no. 1, pp. 29–42, Jan. 1973.
[45] Vivien *et al.*, "Light injection in SOI microwaveguides using high-efficiency grating couplers," *Journal of Lightwave Technology*, vol. 24, no. 10, pp. 3810–3815, Oct. 2006.
[46] "Nanophotonic FDTD Simulation Software - Lumerical FDTD," *Lumerical*. [Online]. Available: https://www.lumerical.com/products/fdtd/. [Accessed: 22-May-2019].
[47] K. Seshan, *Handbook of Thin Film Deposition*. William Andrew, 2001.
[48] S. R. J. Brueck, "Optical and Interferometric Lithography - Nanotechnology Enablers," *Proceedings of the IEEE*, vol. 93, no. 10, pp. 1704–1721, Oct. 2005.
[49] T. Fukasawa, A. Nakamura, H. Shindo, and Y. Horiike, "High Rate and Highly Selective SiO2 Etching Employing Inductively Coupled Plasma," *Jpn. J. Appl. Phys.*, vol. 33, no. 4S, p. 2139, Apr. 1994.
[50] L. Wang, A. B. Mallick, and N. K. Ingle, "Wet oxidation process performed on a dielectric material formed from a flowable cvd process," US20110151677A1, 23-Jun-2011.
[51] N. Barnes, "Dry & Wet Thermal Oxide (SiO2) | 35A - 15um | Custom Film Coatings | SVMI," *Silicon Valley Microelectronics | SVM*. [Online]. Available: https://www.svmi.com/custom-film-coatings/thermal-oxide/. [Accessed: 12-Oct-2019].
[52] J. G. E. Gardeniers, H. a. C. Tilmans, and C. C. G. Visser, "LPCVD silicon-rich silicon nitride films for applications in micromechanics, studied with statistical experimental design*," *Journal of Vacuum Science & Technology A*, vol. 14, no. 5, pp. 2879–2892, Sep. 1996.
[53] "LPCVD furnace." [Online]. Available: https://www.crystec.com/klllpcvde.htm. [Accessed: 12-Oct-2019].
[54] D. N. Wang *et al.*, "Thermal CVD/PECVD reactor and use for thermal chemical vapor deposition of silicon dioxide and in-situ multi-step planarized process," US5000113A, 19-Mar-1991.
[55] "Plasma enhanced chemical vapor deposition - LNF Wiki." [Online]. Available: http://lnf-wiki.eecs.umich.edu/wiki/Plasma_enhanced_chemical_vapor_deposition. [Accessed: 12-Oct-2019].
[56] X. He, S. Benoit, S. R. J. Brueck, and R. Kaspi, "Widely tunable optically pumped mid-IR DFB laser," in *2012 Conference on Lasers and Electro-Optics (CLEO)*, 2012, pp. 1–2.
[57] X. He, S. Benoit, R. Kaspi, and S. R. J. Brueck, "Optically Pumped Continuously Tunable Mid-IR Distributed-Feedback Semiconductor Laser," *IEEE Journal of Quantum Electronics*, vol. 52, no. 10, pp. 1–10, Oct. 2016.
[58] "Si photodiode array S4111-16R." [Online]. Available: https://www.hamamatsu.com/eu/en/product/type/S4111-16R/index.html. [Accessed: 26-Sep-2019].

[59] “CMOS linear image sensor S11639-01.” [Online]. Available: https://www.hamamatsu.com/us/en/product/type/S11639-01/index.html. [Accessed: 26-Sep-2019].